



**HAL**  
open science

# Pressure conditions for shear and tensile failure around a circular magma chamber, insight from elasto-plastic modeling

Muriel Gerbault

► **To cite this version:**

Muriel Gerbault. Pressure conditions for shear and tensile failure around a circular magma chamber, insight from elasto-plastic modeling. The Geological Society, London, Special Publications, 2012, 367 (1), pp.111-130. 10.1144/SP367.8 . hal-01754832

**HAL Id: hal-01754832**

**<https://hal.science/hal-01754832>**

Submitted on 30 Mar 2018

**HAL** is a multi-disciplinary open access archive for the deposit and dissemination of scientific research documents, whether they are published or not. The documents may come from teaching and research institutions in France or abroad, or from public or private research centers.

L'archive ouverte pluridisciplinaire **HAL**, est destinée au dépôt et à la diffusion de documents scientifiques de niveau recherche, publiés ou non, émanant des établissements d'enseignement et de recherche français ou étrangers, des laboratoires publics ou privés.

## Pressure conditions for shear and tensile failure around a circular magma chamber, insight from elasto-plastic modeling

Muriel Gerbault

Université de Nice Sophia-Antipolis, Institut de Recherche pour le Développement (UR 082), Observatoire de la Côte d'Azur, Géoazur, 250 av Einstein 06560 Valbonne, France

Corresponding author (e-mail: [gerbault@geoazur.unice.fr](mailto:gerbault@geoazur.unice.fr))

Number of words of text: 6958

Number of References: 79

Tables: 2

Figures: 8

Appendix : 1

**Abstract:** Overpressure within a circular magmatic chamber embedded in an elastic half space is a widely used model in volcanology. However, this overpressure is generally assumed to be bounded by the bedrock tensile strength, because gravity is neglected. Critical overpressure for wall failure is thus greater. Here, I show analytically and numerically that wall failure occurs in shear rather than in tension, because the Mohr-Coulomb yield stress is less than the tensile yield stress. Numerical modeling of progressively increasing overpressure shows that bedrock failure develops in three stages: (1) tensile failure at the ground surface, (2) shear failure at the chamber wall, and, (3) fault connection from the chamber wall to the ground surface. Predictions of surface deformation and stress with the theory of elasticity break down at stage 3. For wall tensile failure to occur at small overpressure, a state of lithostatic pore fluid pressure is required in the bedrock, which cancels the effect of gravity. Modeled eccentric shear band geometries are consistent with theoretical solutions from engineering plasticity, and compare with shear structures bordering exhumed intrusions. This study shows that the measured ground surface deformation may be misinterpreted when neither plasticity nor fluid pore pressure is accounted for.

An unsolved question in volcanology is that of the conditions for and progression of country rock failure around near-surface, pressurized magma bodies. Anderson (1936) was the first to apply mathematical solutions derived from the theory of elasticity to explain the formation of cone-sheets and ring-dykes around circular igneous intrusions: 'In explaining central intrusions it is necessary to involve both types of rupture, the tensile type to produce cone-sheets, and the shearing-type to account for the production of ring-dykes, giving rise to nearly vertical ring-fractures'. Despite several decades of analytical and numerical models of deformation around magmatic chambers (e.g. reviews by Acocella, 2007; Marti et al., 2008; Geyer & Marti, 2009), and a considerably longer history of field studies examining exposed structures (e.g. Gudmundsson, 2006), there are many open questions left. The crude state of our knowledge with respect to magma chamber deformation is also revealed with the application of elastic models to geodetic monitoring of active volcanoes (e.g. Mogi, 1958; Masterlark, 2007; Segall, 2009). As the non-unique fit between measured and modeled deformation spans a wide range of parameters (chamber geometry, country rock rheology, pore pressure and magmatic overpressure, etc.) it is clear that more constraints are desirable. One fundamental approach is to simulate the failure patterns that arise from an idealistic volcanic chamber with a minimum number of parameters, and such is the objective of this work.

In this paper I show, analytically and numerically, how commonly used solutions of critical overpressure for bedrock failure can be biased when neglecting the role of gravity. Whereas Grosfils (2007) raised this problem of yield stress conditions for tensile failure around a circular magmatic chamber, here I also aim at demonstrating how in fact shear failure should theoretically occur rather than tensile failure. Previous models that use self-consistent elasto-plasticity or visco-elasto-plasticity have not directly addressed the critical pressure condition for bedrock failure. As a matter of fact, the precise state of internal pressure associated with the initiation and propagation of faulting around an idealistic circular magmatic chamber remains poorly constrained.

First, I develop analytically the conditions for failure around a circular pressurized inclusion. Then, the reasoning is supported with numerical models that incorporate self-consistent elasto-plasticity with a Mohr-Coulomb failure criterion. I explore the progression of plastic yielding, displaying peculiar geometrical patterns that are produced with increasing internal overpressure, and I show their similarity to solutions from engineering plasticity. The role of fluid pore-pressure is also illustrated, as it nullifies the gravity component in the shear failure yield criterion, and allows for tensile failure to occur instead.

In discussing conditions for shear failure in the real world, a few examples of shearing structures exposed at the borders of magmatic bodies are displayed. In order to explain field observations of tensile failure, which were predicted to occur for less than or an average of 10 MPa of internal overpressure, the main point of this paper is to show that if this is the case (around an ideal spherical magmatic chamber), then it is necessary to consider a state of near-lithostatic fluid overpressure in the bedrock.

## **Analytical pressure solutions for tensile and shear failure**

### **Classical solution for tensile failure**

Simple solutions of surface displacement over a spherical source, with depth much greater than radius, were approximated by Mogi (1958) using a dilational point source. This solution remains widely used for fitting geodetic measurements above active volcanoes (Bonafede et al., 1986, 2009; Masterlark and Lu, 2004; Masterlark, 2007; Ellis et al., 2007; Pritchard and Simons, 2004; Trasatti et al., 2005; Foroozan et al., 2010). Crustal deformation in the idealistic elastic crust is assumed to be the result of a pressure change  $\Delta P$  in the source with respect to “hydrostatic” pressure. Assuming Poisson’s ratio ( $\nu$ ) is equal to 0.25 and  $G$  is the shear modulus, calculated horizontal and vertical displacements at the surface are:

$$u_x = \frac{3 \Delta P}{4 G} \cdot \frac{R^3 \cdot x}{(x^2 + H^2)^{3/2}}, \quad u_y = \frac{3 \Delta P}{4 G} \cdot \frac{R^3 \cdot H}{(x^2 + H^2)^{3/2}}. \quad (1)$$

where  $R$  and  $H$  are the radius and the depth of the chamber, respectively (**Fig. 1**). In plane-strain, the magma chamber becomes an infinitely long cylinder, and the analytical solution differs by a factor of about 4 depending on  $R$  and  $H$ ; stress functions for a generic class of problems with complex variables are provided by Verruijt (1998).

The distribution of the stress field produced by a pressurized circular cavity in an elastic half-space was solved by Jeffery (1920) using curvilinear coordinates and plane-strain. At the free surface, he showed that the horizontal component of the stress field ( $\sigma_{xx}$ ) is :

$$\sigma_{xx} = \frac{-4 \Delta P \cdot R^2 \cdot (x^2 - H^2 + R^2)}{(x^2 + H^2 - R^2)^2}. \quad (2)$$

Its maximum is located above the chamber at  $X_0$ , with  $\sigma_{xx} = 4 \cdot \Delta P \cdot R^2 / (H^2 - R^2)$ . At the chamber wall, the hoop stress is expressed according to either the angle  $\alpha$  between the vertical axis of symmetry and the line joining the surface origin  $X_0$  to a point on the chamber wall (Jeffery, 1920), or to the polar angle  $\theta$  taken from the horizontal at the chamber's center to that same point (Grosfils, 2007):

$$\sigma_{\theta\theta} = \Delta P \cdot (1 + 2 \tan^2 \alpha). \quad (3)$$

Jeffery (1920) defined the free surface correction factor  $C = 1 + 2 \tan^2 \alpha$ , and showed that the hoop stress at the wall is maximum when  $\alpha_m = \arcsin(R/H)$  (**Fig. 1**). Then,  $\sigma_m = -\Delta P \cdot (H^2 + R^2) / (H^2 - R^2)$ .

Jeffery (1920) also discussed the conditions for failure: "if  $H$  is greater than  $R\sqrt{2}$  and less than  $R\sqrt{3}$ , and internal pressure increased until failure occurs, the crack will begin on the surface according to the greatest tension theory, or on the edge of the hole if the greatest stress-difference theory holds".

A majority of authors, such as Pinel and Jaupart (2003, 2005), Gudmundsson (1988), Gudmundsson et al. (1997) and Tait et al. (1989), assume that the same tensile failure criterion applies to the Earth's surface and the chamber walls, that is when the deviatoric stress ( $\frac{1}{2}(\sigma_1 - \sigma_3)$ ) exceeds the rock's tensile strength,  $T$  :

– at the surface where the gravity component vanishes, failure occurs when  $\frac{1}{2}(\sigma_{xx} - \sigma_{zz}) = T$ , therefore combined with (3), when the internal overpressure reaches the critical value

$$\Delta P_s = T \cdot (H^2 - R^2) / 2R^2. \quad (4)$$

– at the chamber wall, the same tensile failure criterion gives  $\frac{1}{2}(\sigma_{\theta\theta} - \Delta P) = T$ . Therefore combined with (2), the critical internal overpressure is

$$\Delta P_T = T \cdot (H^2 - R^2) / H^2. \quad (5)$$

Thus, tensile failure is traditionally predicted to initiate at the previously given location  $\alpha_m$  along the chamber wall for magmatic overpressures  $\Delta P_T \leq T$ , which ranges in between ~6 MPa (Gudmundsson et al., 2002) and 20 MPa (Pinel & Jaupart, 2003).

### **Grosfils' solution for tensile failure**

Grosfils (2007) demonstrated analytically and numerically that a higher critical overpressure was required to initiate wall failure, invoking the necessity to account for the gravity body force. Considering a spherical chamber of equal magma and rock densities, his analytical reasoning is summarized below:

(a) the total magma pressure is first defined as the sum of an internal overpressure  $\Delta P$  and the lithostatic stress,  $P_t = \Delta P - \rho g y$ .

(b) Grosfils (2007) then proceeded as previous studies (e.g. Gudmundsson, 1988), in assuming that the tangential stress  $\sigma_{\theta\theta}$  equals half the normal stress balance across the wall modified by the free surface factor (C), so that :

$$\sigma_{\theta\theta} = C \cdot \Delta P / 2. \quad (6)$$

(c) Grosfils (2007) expressed  $C$  as a function of relative depth  $h$  taken from the crest of the chamber, itself located at depth  $D=H-R$  (**Fig. 1**) :

$$C = 1 + 2 \tan^2 \alpha = \frac{2h \cdot (2R + D) + D^2 - h^2}{(D + h)^2}. \quad (7)$$

$C$  has a parabolic shape  $>1$ , and equals 1 when  $h$  equals 0 or  $2R$ .

(d) then, to the difference of previous authors, Grosfils (2007) argued that tensile failure at the chamber's wall occurs when the tangential stress  $\sigma_{\theta\theta}$  exceeds not only the tensile strength of rocks ( $T$ ), but also the wall-parallel component of the lithostatic stress ( $P_l$ ):

$$\sigma_{\theta\theta} = T + P_l = T + \rho g(D + h). \quad (8)$$

(e) Combining equations (6), (7) and (8), Grosfils's overpressure for tensile failure  $\Delta P = \Delta P_{TG}$  is

$$\Delta P_{TG} = 2T / C + 2 \rho g \cdot (D + h) / C. \quad (9)$$

In summary, « the total pressure  $P_t$  required for tensile failure approaches the limit of 3 times the lithostatic stress  $\sigma_z$  at great depth ( $D \gg R$ ), whereas it becomes less than  $\sigma_z$  if  $R > 0.6D$ » (Grosfils, 2007). The associated critical overpressure  $\Delta P_{TG}$  contrasts with the prediction of  $\Delta P_T$  of failure for only a few MPa above lithostatic (Eq. 5, e.g. Tait et al., 1989; Gudmundsson et al., 1997, 2002; Pinel and Jaupart, 2003, 2005; Gudmundsson, 2006). Grosfils discussed in detail how this difference stems from the absence of gravity in the formulation of most analytical models; and contrarily to common saying, 'a self-consistent numerical approach that incorporates explicitly boundary stresses and body loads becomes a necessary reference against which analytical models should be improved'.

### Conditions for shear failure

Now we shall evaluate the internal overpressure ( $\Delta P_{MC}$ ) necessary to produce shear

failure in the bedrock surrounding the chamber, and compare it with the above-mentioned overpressure prediction required for tensile failure.

The classical Mohr-Coulomb criterion of failure relates the tangential and normal stresses  $\tau_s$  and  $\sigma_n$ , along any given plane of a medium with internal friction angle  $\varphi$  and cohesion  $S_o$ . This criterion can also be written in terms of the pressure  $P$  and the deviatoric shear stress  $\sigma_{II}$  :

$$\tau_s = S_o - \tan\varphi \cdot \sigma_n, \quad \tau_s = \sigma_{II} \cos\varphi, \quad \sigma_n = -P + \sigma_{II} \sin\varphi. \quad (10)$$

We first neglect gravity, and assume that the minimum and maximum principal stress components at the chamber's wall are of opposite sign, so that  $P=0$ , and  $\sigma_{II} = \Delta P_{MC}$  ( $\Delta P_{MC}$  is the applied internal overpressure; note that instead in 3D,  $\sigma_{II} = \Delta P_{MC}/2$ , Timoshenko & Goodier, 1970). When adding gravity, the isotropic lithostatic component appears in the total pressure  $P = -\rho gy$  (at negative depth  $y$ ) which, when inserted into (10), provides :

$$\Delta P_{MC} = S_o \cos\varphi - \rho gy \cdot \sin\varphi. \quad (11)$$

In order to account for the free-surface (e.g. Gudmundsson, 1988; Parfitt et al, 1993), the factor  $C$  appears in the relationship between the principal stresses at the wall:  $\sigma_3 = -C \cdot \sigma_1$ . Then the stress invariants  $P$  and  $\sigma_{II}$  are expressed as:  $P = -\rho gy + \Delta P \cdot (C-1)/2$ ,  $\sigma_{II} = \Delta P \cdot (C+1)/2$ .

Inserting these expressions into the Mohr-Coulomb criterion (Eq. 10), and defining a theoretical tensile strength deduced from the cohesion,  $T_o = S_o / \tan \varphi$ , provides the critical overpressure required for shear failure  $\Delta P_{MCS}$  :

$$\Delta P_{MCS} = 2 \sin \varphi \cdot \frac{-\rho gy + T_o}{1 + \sin \varphi + C \cdot (1 - \sin \varphi)}. \quad (12)$$

At the vertical axis of symmetry, where  $C = 1$ , this expression returns to Eq. 11.

Figure 2 displays all three analytical predictions of the internal pressures required for

a) tensile failure at the chamber wall according to classical predictions (cf. Eq. 5), b) Grosfils' prediction (cf. Eq. 9), and c) shear failure according to Eq. 12. Friction and cohesion are defined as  $\varphi = 30^\circ$ ,  $S_o = 10$  MPa. Two cases with different depth and radius are displayed, one at depth  $H = 7$  km and radius  $R = 2$  km ( $R/D=0.4$ ), and another at depth  $H = 2$  km and  $R = 1$  km ( $R/D=1$ ). For both cases, the critical overpressure for shear failure ( $\Delta P_{MC}$ ) is smaller than that for tensile failure when gravity is accounted for. The effect of the free-surface modifies only the internal slope between the crest and the base of the chamber, which indicates that shear failure can initiate over a broad domain extending laterally from the chamber roof.

In summary, I have shown that a chamber wall should yield by shear failure (mode II) rather than by tensile failure (mode I).

### **Predictions from other studies**

Many studies have developed analogue and numerical models of failure around a magmatic chamber (e.g., Roche, 2001; Acocella, 2004, and see reviews by Acocella, 2007, and Marti et al., 2008) but surprisingly, apart from Grosfils (2007), few directly address the association between the mode of failure, the geometry of the failure domain and the internal overpressure. There are several methodological reasons for this:

(a) First, a majority of studies model only elastic behaviour of the bedrock, and contour the domains that exceed a failure stress threshold that is chosen a priori (e.g. Sartoris et al., 1990; Gudmundsson, 1988, 2002, 2006; Masterlark, 2007). This method has been used since the 1950's (Hafner, 1951) but, while it generally yields good results to a first order, it does not account for self-consistent plasticity. This method therefore cannot address when exactly failure initiates with respect to the level of internal magmatic overpressure.

(b) Other models incorporate self-consistent elasto-plasticity, but a dilational deformation is applied instead of an internal overpressure (Chery et al., 1991; Kusumoto & Takemura,

2003; Gray and Monaghan, 2004; Hardy, 2008). Only Chery et al. (1991) evaluate chamber overpressures of 50-60 MPa around a magmatic chamber 10 km deep embedded in a temperature dependent elasto-plastic-ductile crust; however, a state of hydrostatic pore fluid pressure was also assigned in the bedrock, and the precise shape of the associated failure domain was not given (the mesh resolution was poor with a chamber wall composed of 12 elements).

(c) Models that define a magmatic chamber with sharp edges produce failure much « more easily » than when an ideal circular body is used. For example, Burov & Guillou-Frottier (1999) and Guillou-Frottier et al. (2000) modeled a cycle of inflation and collapse with only 10 MPa overpressure, applied in a middle-crust rectangular chamber, with visco-elasto-plastic rheology. In these models, shear band structures develop between the corners of the chamber and the surface.

(d) Finally, Trasatti et al. (2005) tested a number of parameters to model surface uplift at Campi Flegrei volcano. Whereas Mogi-type elastic models without gravity reproduced the measured uplift for an internal overpressure of at least 80 MPa (the lithostatic pressure at the chamber's crest  $D \sim 3200$  m, recognized as unrealistic), elasto-plastic models including gravity and a Von Mises failure threshold set to 15 MPa, reproduced the uplift for an internal overpressure of only 45-50 MPa. This study illustrates how greater surface uplift is obtained when accounting for shear failure, and for a 'reasonable' overpressure greater than the tensile strength (note that this overpressure fits Eq. 12 at the crest,  $\sin(30) \cdot (\rho g D + T) \sim 48$  MPa). Unfortunately the geometrical pattern of bedrock failure was not shown in this study.

### **The point of view of engineering plasticity**

In engineering mechanics, a problem similar to a magmatic chamber is that of a pressurized cavity, applied to metal indentation and tunnelling. A technique known as slip-line field theory is used. Nadai (1950), for example, displayed the slip-lines solution associated with the indentation of an infinite plastic medium (**Fig. 3a**). Defining the radial and tangential

normal principal stresses  $\sigma_r$  and  $\sigma_\theta$ , and  $k$  as Tresca's yield stress, the plasticity condition reduces to  $\sigma_r - \sigma_\theta = \pm 2k$ , and solutions take the form:  $\sigma_r = \pm 2k \cdot \ln(R/r), \sigma_\theta = \pm 2k \cdot (1 + \ln(R/r))$ . The resulting slip lines are two orthogonal families of logarithmic spirals, commonly observed in steel plates pressed against a cylindrical stamp.

Prediction of plastic flow patterns for the even « simpler » problem of flat indentation remains difficult because there are many possible slip systems. Closed-form kinematical solutions for flat indentation were calculated by Salençon (1969, **Fig. 3b**) and will be used further at the end of this paper. A lower bound for the internal pressure associated with failure around a cylindrical cavity was provided by Salençon (1966), whereas Caquot (1956) and d'Escatha and Mandel (1974) analyzed the static admissible stress field for an upper bound using various friction and cohesion values. D'Escatha and Mandel presented graphical solutions based on the slip-line characteristics method (shown in **Fig. 3c**), and Caquot (1956) provided closed-form solutions. Fairhurst & Carranza-Tores (2002) used the numerical code FLAC to simulate a progressively decreasing support pressure on the wall of a circular tunnel, and observed that failure did not start until the pressure was reduced to 80% of Caquot's (1956) upper bound value.

More recently, Massinas & Sakellariou (2009) provided another closed-form solution of the critical support pressure  $P_{cr}$  for wall failure around a tunnel. Bipolar coordinates  $\alpha$  and  $\beta$  were used similarly to Jeffery (1920), in which  $\alpha_1 = \text{csh}^{-1}(H/R)$ . Here,  $P_o$  is defined as the uniform external pressure (set as a proxy to the gravity load at the cavity's center), and the Mohr-Coulomb friction angle  $\varphi$  is defined as before. Failure occurs at the wall for the minimum value of internal support pressure  $P_{cr}$ , which occurs when coordinate  $\beta$  equals 0 at the tunnel crest:

$$P_{cr} = \frac{P_o(1 - \sin\varphi)(1 + \sin^2\beta / \sinh^2\alpha_1) - T_o \sin\varphi}{1 + (1 - \sin\varphi) \sin^2\beta / \sinh^2\alpha_1}, \quad (13)$$

*For  $\varphi = 30^\circ, \beta = 0, P_{cr} = P_o / 2 - T_o / 2.$*

Note how this critical overpressure compares with the one that was calculated in Eq. 11: it is equal when considering, first, that signs are opposite for a depressed cavity and for

an inflating chamber, and second, that the integrated average of a linearly increasing pressure with depth corresponds to half the maximum pressure  $P_o$ .

According to Massinas & Sakellariou (2009) and references therein, for deep tunnels with  $H/R \geq 7$ , the geometry of the plasticized domain is circular around the tunnel as the effect of the free-surface is less than 10%. For shallow tunnels with  $H/R < 7$ , the geometry of the plasticized domain becomes eccentric, displaying the shape of «ears» (**Fig. 3d**).

### **The role of pore-fluid pressure**

The role of pore fluid pressure in volcanic systems has long been thought to contribute to complex mechanisms such as heating of confined pore water by intrusions, degassing of intrusions, discharges of highly pressurized fluids from depth, or deformation by faulting (e.g. Day, 1996). Here, we will use a very simple assumption of the role of pore fluid pressure in the bedrock, and argue how it can yet play a fundamental role in the mode of fracturing around magmatic chambers. Hubbert & Rubey (1959) proposed that fluids in pores produce an effective normal stress  $\sigma_{\text{eff}} = \sigma_n - p_f$ , that is involved in the Mohr-Coulomb yield criterion as:

$$\tau = S_o - \tan(\phi) \cdot (\sigma_n - p_f). \quad (14)$$

Hubbert and Rubey (1959) expressed  $p_f$  in terms of the vertical lithostatic stress and the pore-fluid pressure ratio  $\lambda$ , so that  $p_f = -\lambda \cdot \rho g y$ . In a rock of density  $2500 \text{ kg/m}^3$ ,  $\lambda = 0.4$  for hydrostatic pore fluid pressure, and  $\lambda = 1$  for lithostatic pore fluid pressure. While Townend and Zoback (2000) argued convincingly that hydrostatic pore fluid pressure appropriately describes an equilibrium state within the crust, lithostatic pore fluid pressure may also be relatively common in nature since many well data indicate values of  $\lambda$  equal to  $0.9$  (Engelder and Leftwich, 1997; Hillis, 2003). If we consider this extreme case of lithostatic fluid pore pressure in the bedrock surrounding a magmatic chamber, then the component of gravity is cancelled out in the failure criterion (Eq. 14), and wall failure at the chamber wall can then be

evaluated without accounting for this body force (Eq. 5 becomes valid again).

If one can justify the development of up to lithostatic pore fluid pressures in the neighbourhood of a magmatic chamber, then shear and tensile failure are predicted to occur under relatively small internal overpressures of the order of the tensile strength of rocks (10 MPa).

Thus, a state of lithostatic pore fluid pressure surrounding magmatic chambers should be envisaged when field observations report a majority of mode I opening dykes (e.g. Gudmundsson, 2006). This point will be further discussed at the end of this study.

## **Numerical modeling of inflating magma chambers**

### **Numerical method and setup**

The finite-differences code Parovoz is used (Poliakov and Podladchikov, 1992; Podladchikov et al., 1993), which is based on the FLAC method (Cundall and Board, 1988). In this method the equations of motion are solved explicitly in time and in large strain mode, retaining a locally small strain formulation commonly used in continuum mechanics. This method is well known to be able to reproduce the initiation and propagation of non-predefined faults (treated as shear bands, e.g. Poliakov and Podladchikov, 1992), and it has been used in a number of geodynamical settings (e.g., Lavier et al., 2000, Burov & Guillou-Frottier 1999, 2003; Gerbault et al., 1999). The program executes the following procedure in one time-step. Velocities are first calculated from the equation of motion with density  $\rho$ , time  $t$ , velocity vector  $V$ , stress tensor  $\sigma$  and gravity acceleration  $g$ :

$$\rho \, dV_i/dt + d \, \sigma_{ij}/dx_i = \rho \, g \quad (15)$$

where  $d/dt$  and  $d/dx_i$  are the time and space derivatives. Deformation rate is:

$$\varepsilon_{ij} = 1/2(dV_i/dx_j + dV_j/dx_i) \quad (16)$$

and is used to calculate the new stress distribution from the elasto-plastic constitutive law. From these new stresses, nodal forces and displacements are evaluated and inserted in the next time-step. Elasticity relates stress and strain with Lamé parameters  $\lambda$  and  $G$  ( $\delta_{ij}$  is the Kroenecker symbol):

$$\sigma_{ij} = \lambda \cdot \varepsilon_{ij} + 2G \varepsilon_{ij} \cdot \delta_{ij} \quad (17)$$

Non-associated plastic flow is modeled (e.g. details in Cundall, 1989; Gerbault et al., 1998; Kaus, 2010) with a frictional Mohr-Coulomb stress criteria given in Eq. 10 and a dilatancy set to 0 (Vermeer and de Borst, 1984). Common failure parameters are chosen, with friction  $\varphi=30^\circ$ , cohesion  $S_0=10$  MPa, and tensile cutoff strength  $T=5$  MPa. Modeled shear bands are commonly assimilated to shear « faults ». Tensile failure is detected when one or more stress components exceeds the tensile cutoff  $T$ . Despite Parovoz being a two-dimensional plane-strain code, the condition for failure is evaluated with the three stress components. Although Parovoz can identify domains of tensile failure, the mesh continuum cannot split such as in real mode I crack opening. However, White et al. (2004) successively compared domains of tensile failure identified by FLAC<sup>2D</sup>, with a Particle Flow Code that can track individual microfractures via breakable bonds.

Our problem is modeled in plane-strain. The left border ( $X=0$ ) represents the vertical axis of symmetry passing through the center of a circular magma chamber. Domain dimensions are 100 km in length and 80 km in depth, far enough from the zone of interest to minimize border effects. The chamber has radius  $R=2$  km and is located at  $H=7$  km depth.

The mesh is defined with quadrilateral elements of height and width equal to 25 m over the first 12 km of the model domain. Grid resolution progressively reduces in both directions to approximately 1 km at the bottom right corner. The total number of mesh elements is 275,000.

In the model, all borders apart from the free ground surface have free-slip boundary

conditions. A uniform rock density is set with  $\rho = 2500 \text{ kg/m}^3$  (Table 1 summarizes all analytical and numerical variables). The model is initially set up with isotropic lithostatic components (weight of overburden rocks), so that a strain of only 1‰ develops during readjustment to the plane-strain conditions (e.g. Turcotte and Schubert, 1982).

In the Appendix, numerical benchmarks of the results that are described in the following sections are displayed. The formation and development of precise shear bands is conditioned by a sufficiently high mesh resolution, which requires computationally expensive runs. The major numerical concern is mesh-locking effects as shear bands form and propagate from the chamber wall. The finite element code Adeli (Hassani et al., 1997; Chery et al., 2001) is used to benchmark our solutions. The benchmark shows the effects of meshed versus unmeshed chamber, and of coarse mesh resolution especially when the domain becomes highly plasticized. Localizing plastic deformation is well known to be complicated to model numerically (e.g. Yarushina et al., 2010). Thus, I make a call to the community in order to improve this benchmark with high resolution models, similar perhaps to those that have been conducted for the problem of fault propagation in accretionary prisms (Buiter et al., 2008).

### **Assumptions about the rheological behavior of the chamber**

Many models of an inflating magmatic chamber do not include the internal domain of the magmatic chamber in their mesh. However, I included it in the model domain in order to achieve high mesh resolution with the quadrilateral elements formulation of Parovoz. The rheology of the chamber must thus be defined with Lamé parameters. While a magmatic chamber filled with low viscosity fluid should be assumed incompressible (Poisson's ratio=0.5), many studies point to the important proportion of volatile phases, which reduce both its elastic rigidity and its incompressibility (Bower & Woods, 1997; Huppert & Wood, 2002; Rivalta & Segall, 2008). The effect of the elastic properties of the chamber were thus

preliminarily verified. The greater the internal Young's modulus, the more the chamber dilates and «absorbs» its internal pressure, thus transferring less pressure to the outer walls and bedrock domain. The pressure felt out of the chamber walls is thus best measured via the second invariant of the deviatoric shear stress, similar to the approach used by Chery et al. (1991).

If the Young's modulus is diminished to 10 times that of the external bedrock, then more than 90% of the applied internal pressure is transferred to the outer domain. In this case, the value of Poisson's ratio does not act significantly. The tests show that modeled stress and deformation become indistinguishable for models with  $\nu = 0.25$  and  $\nu = 0.45$ . The presented reference model assumes Lamé parameters equal to 1/20 those outside the chamber (corresponding to  $\nu = 0.25$ ,  $E = 2.5$  GPa, whereas in the bedrock  $E = 50$  GPa).

Numerical experiments follow a procedure in which the internal overpressure ( $\Delta P$ ) increases progressively. This pressure increase occurs proportionally to the time-step of the model, according to  $\Delta P = A * time$ ;  $A$  is a coefficient fixed so that the pressure increases fast enough for the total computing time of the run to be reasonable, and slow enough so that deformation resulting from a specific  $\Delta P$  detected during our sampling frequency provides a quasi-static solution. Application of an internal overpressure that overshoots the yield strength of elements can lead to numerical inconsistencies. This justifies the application of a continuous radial deformation to model magmatic inflation (e.g. Chery et al., 1991). However, for the specific purpose of our study, application of a radial overpressure is more appropriate (as in tunnelling engineering, see above).

In the real world, the onset of an eruption or dyke injection releases confined magmatic fluids from the chamber, and therefore inhibits further increase in internal overpressure. However, Wegler et al. (2006) interpreted continuously increasing shear wave velocities below the Merapi volcano as an indicator of increasing magmatic pressure in between two consecutive eruptions in 1998. The application of an elevated internal

overpressure in our models should therefore be considered within the context of rapid arrival of over-pressurized magma, and as a preliminary stage of regional micro-cracking and damaging of the host rock, prior to the onset of dyke injection or magmatic eruption (see discussion section).

## **Different stages of deformation with increasing pressure**

Sequential results of a reference model (M1 in Table 2) are presented **Fig. 4** at increasing internal overpressure. Zones of failure, shear strain, deviatoric and horizontal stresses are described below for three different stages of evolution.

### **Stage 1: Development of surface tensile failure ( $\Delta P_1$ )**

Internal overpressure increases progressively from an initial uniform lithostatic state. Tensile failure is first reached at the origin  $X_0$  on the ground surface, and expands progressively both in width and depth. Since this surface is defined as stress free, failure is only limited by the equality of  $\sigma_{xx}$  with the tensile strength  $T= 5\text{MPa}$ . Locally, the horizontal stress is slightly higher, with  $\sigma_{xx}= 6\text{ MPa}$ , because of values taken at the center of 25 meters-thick mesh elements.

The analytical prediction (Eq. 4) without gravity provides failure at the surface for  $\Delta P_1 = T \cdot (H^2 - R^2) / 2R^2 = 28.13\text{ MPa}$ . The numerical model produces surface rupture in between  $27.4 < \Delta P_1 < 28.4\text{ MPa}$  (numerical time-step sampling is automatic and cannot correspond to exact critical analytical pressures). The consistency of the numerical value of  $\Delta P_1$  with the analytical solution of Eq. 4 indicates that failure at the surface is less dependent on the gravitational load acting on the system than on the local state of stress at the very top surface where gravity stresses vanish.

## Stage 2: Development of shear failure along the chamber wall ( $\Delta P_2$ )

As internal overpressure continues to increase, tensile failure ceases to propagate, and is replaced by normal shear faults that also propagate downwards. Shear failure then initiates around the chamber (**Fig. 4b**). The numerical model indicates that this occurs at an overpressure of 70 MPa, in excellent agreement with the Mohr-Coulomb yield prediction evaluated in Eq. 11:  $\Delta P_{MC} = (-\rho g y + T_0) \cdot \sin \phi = 71 \text{ MPa}$ .

Shear failure first initiates in the upper quarter of the chamber wall, consistent with analytical predictions and Figure 2. With increasing overpressure, shear-bands initiating at the chamber wall are oriented at an angle  $45 \pm \phi/2 = 30^\circ$  to the most compressive radial direction, in agreement with expectations for a non-associative Mohr-Coulomb material (e.g. Vermeer & de Borst, 1984; Kaus, 2010). These shear-bands develop eccentrically from the chamber, and cross each other at an angle of  $60^\circ$  consistent with a friction angle  $\phi = 30^\circ$  (e.g. Vermeer & de Borst, 1984; Gerbault et al., 1998; d'Escatha & Mandel, 1974). Note that the difference in orientation between these modeled shear bands and those calculated by d'Escatha and Mandel (1974, friction angle  $\phi = 20^\circ$ , **Fig. 2**) stems from perpendicularly orientated principal compressive stresses due to the application of either an overpressure (this study) or an underpressure (d'Escatha and Mandel, 1974).

## Stage 3: Faults connection and possible secondary chamber

With increasing overpressure, outward dipping shear and reverse faults expand from the chamber upwards, simultaneously with inward dipping normal faults that propagate from the surface downwards. These two plasticized (i.e. faulted) domains eventually connect and merge (**Fig. 4c**). The connection occurs at a depth  $d_m$  along the vertical axis of symmetry as a function of the chamber width and depth (R and H). This depth  $d_m$  compares with a typical distance at which slip-lines cross each other in analytical solutions for flat indentation of a perfectly plastic material (Salençon, 1966, distance OJ, **Fig. 2b**). I shall return to this point in the discussion part of our study, and speculate that this local dilation zone, where deep and

shallow shear zones connect, may focus a secondary magmatic reservoir close to the surface.

This 3<sup>rd</sup> stage, where the domains of plasticized material connect the chamber to the surface, occurs when  $\Delta P$  reaches about 130 MPa in the model. The possibility to achieve such a high overpressure seems extreme in a quasi-static situation; however, such high overpressures may occur as a transient phenomenon if one considers extremely rapid arrival of over-pressurized magmatic fluids, which have no time to relax within the chamber.

Whereas failure at the chamber wall initiates over the crest domain, consistent with analytical predictions illustrated in Fig. 2, most active shear bands depart from the chamber wall at the angle interval  $\theta \sim 45-60^\circ$  from the horizontal direction taken at the chamber center. Our explanation for a greatest intensity of localized deformation at this location is the following. Above the crest of the chamber, principal stresses rotate by  $90^\circ$ , and shear bands that propagate to the surface must rotate as well, cross each other and reflect on the vertical axis of symmetry. Instead, at  $\theta \sim 45-60^\circ$ , changes in stress orientations are minimal in the domain between the chamber wall and the top surface, thus favoring the formation of straight shear bands expanding from the chamber to the surface, which form eventually at the final stage of the model (**Fig. 3d**). Therefore, the geometry of failure results from a dynamic mechanism of deformation that minimizes work between the chamber and the surface, rather than depending solely upon the local stress minima (e.g. Masek & Duncan, 1998, applied the minimum work principle to mountain building). In addition, note that shear bands initiating at  $\theta \sim 60^\circ$  at the chamber wall also form at  $30^\circ$  from the most compressive stress (radial), and are thus naturally oriented at  $60+30=90^\circ$ , e.g. the vertical, and closely parallel to the mesh's « fabric ».

When plotting surface displacements at different time-steps (**Fig. 5a**) and also as a

function of time (**Fig. 5b**), departure from a linear elastic increase in surface uplift is seen to become significant after Stage 3, when the failure domain is connected from the chamber to the surface.

## The effect of fluid pressure on bedrock deformation

I argued analytically above that the presence of pore-fluid pressure  $p_f$  would enable failure for significantly lower internal overpressures because it annihilates the gravity component in the yield stress criterion. I shall now illustrate this effect with numerical models by taking into account fluid pore-pressure in the yield stress criterion.

Two sets of models are performed using Parovoz, in which the yield criterion is expressed according to Eq. 14, with a constant bedrock pore fluid pressure set first to hydrostatic ( $\lambda = 0.4$ ) and then to lithostatic ( $\lambda = 1$ ).

When accounting for a hydrostatic pore-fluid pressure ( $p_f = \rho_w g y$ ,  $\lambda = 0.4$ ) in the bedrock, the progressive increase in internal overpressure leads to a first stage of tensile and normal faulting at the surface, followed by the initiation of shear failure at the chamber wall (stage 2), at an overpressure consistent with the analytical prediction  $\Delta P_{MC} = \sin \varphi \cdot (T + (\rho_f - \rho_w) g D) = 43$  MPa. **Fig. 6a** displays a snapshot of this model at 54 MPa, where one notices the initiation of shear failure at the chamber wall (blue dots).

When accounting for a lithostatic fluid pressure ( $p_f = \rho_r g y$ ,  $\lambda = 1$ ) in the bedrock, the onset of wall shear failure is predicted when  $\Delta P_{MC} = \sin \varphi \cdot T_o$ , according to Eq. 11. Thus, if tensile strength  $T = T_o = S_o / \tan \varphi = 17.3$  MPa (there is no cutoff), then  $\Delta P_{MC} = 8.6$  MPa. The onset of wall tensile failure is predicted from Eq. 5 when overpressure  $\Delta P_T = T \cdot (H^2 - R^2) / H^2$ . Thus in the case where the tensile strength  $T = 17.3$  MPa, tensile failure cannot occur since  $\Delta P_T = 15.9$  MPa, which is greater than  $\Delta P_{MC}$ . However, if tensile strength  $T = 5$  MPa, tensile failure is predicted at the wall for  $\Delta P_T = 4.6$  MPa, which is lower than  $\Delta P_{MC}$ .

The numerical results are consistent with these predictions. With a tensile strength cutoff  $T = 5$  MPa, the numerical model produces tensile failure at the wall, and before any failure occurs at the ground surface (**Fig. 6b**). The plasticized domain has an almost circular shape; subsequent increase in internal pressure increases its radius, with connection with the surface taking the shape of an amphora (not shown).  $\Delta P$  needs to reach 21 MPa so that the plastic domain branches to the surface.

Another model is displayed in **Fig. 6c**, in which the bedrock is again assumed to be at lithostatic pore fluid pressure but for which there is no prescribed tensile strength cutoff (therefore  $T = T_o = S_o / \tan \phi = 17.3$  MPa). In this case, shear failure is shown to develop throughout the bedrock, with a precise onset at the wall when  $\Delta P = 8.6$  MPa (as predicted above).

Table 2 lists the fracturing stages and values of surface uplift for these models with hydrostatic and lithostatic pore-fluid pressure and shows that, for internal pressures equivalent to model M1, the fracturing pattern occurs systematically a stage ahead and is associated with greater deformation than in model M1.

## **Discussion of the models with respect to geological observations**

### **Shear fracturing around exposed intrusions, open faults and fluids**

Many field observations report mode I opening structures, mainly dyke intrusions, as a dominant process of deformation outside magmatic bodies (e.g. Gudmundsson, 2006; Holohan 2010). However, geological studies also report shear faulting prior to dyke intrusion. **Figure 7** illustrates such observed shear structures.

The Solitario Laccolith, Trans-Pecos Texas, is a 16 km diameter dome that displays a complex sequence of doming, with sill and dyke intrusions that were mapped and dated by Henry et al. (1997). They interpreted quartz-phyric rhyolite dykes (their Tir4) to have intruded along radial and concentric shear fractures during doming (**Fig. 7a**).

Arran Island, Scotland, is a typical reference for preserved structures formed during magmatic intrusion (**Fig. 7b**). Describing these, Woodcock & Underhill (1987) note how 'late in the intrusion history of the Paleocene Northern granite, the major faults (in Permian-Triassic New Red Sandstones) on the southeast side of the granite formed a conjugate strike-slip system that accommodated radial expansion of the pluton'.

A 30 cm-scale rock is displayed in **Fig. 7c**, which was sampled along the track of the Glen Rosa valley, Arran. The grey part of this rock (the "bedrock") displays a regular pattern of conjugate shear bands crossing each other at  $\sim 60^\circ$ , adjacent to another unfaulted domain of whiter colour, presumably the "fluid." One of these shear bands (A) has been infiltrated by that fluid, and is about 2 mm thick. About 20 cm to the right, another much thicker ( $\sim 2$  cm) limb of fluid expands through the "bedrock" and overprints the conjugate system of faults (B). This observation may be interpreted as follows: first, shear fracturing has developed "pervasively" in the bedrock surrounding an over-pressurized medium (which did not fail); then, the fluid infiltrated the shear-bands, prior to or contemporary with a more massive event in which tensile opening expelled greater amounts of fluid throughout the "bedrock."

Other independent observations argue in favor of the occurrence of shear fracturing around magmatic chambers. First, in a general context of extension excluding fluid involvement, it is well known that tensile stress does not systematically lead to mode I opening. For example, Ramsey & Chester (2004) showed from laboratory experiments under triaxial tension, that rock failure can evolve continuously from mode I opening cracks to mode II shear fractures as the confining pressure increases. Second, the observation of seismicity under volcanic edifices indicates double-couple earthquake focal mechanisms, associated with or prior to an eruption (e.g. Ruiz et al., Magma volume calculations at Tungurahua Volcano, AGU Meeting of the Americas, Foz do Iguassu, 2010; Waite & Smith, 2002). Double-couple focal mechanisms are an indicator for failure occurring in mode II, independently of the well recognized presence of large amounts of fluids in active volcanic zones.

The present analytical and numerical study indicates that the occurrence of mode I fracturing around an inflating magmatic chamber requires that the bedrock medium contains sufficient fluid pore pressures close to a lithostatic state. It suggests that, once the bedrock around an inflating chamber is pervasively, sufficiently weakened by either processes of shear fracturing, micro-cracking, or transport of fluids in pores associated with the inflation, can the subsequent massive stage of mode I fracturing occur by means of dyke or sill emplacement and eruption. A more complex dynamic model accounting for double phase hydro-mechanical processes is required to demonstrate the validity of such mechanisms.

### **Insights from the modeled failure geometry**

The sophisticated faulting geometries obtained in the numerical experiments (stage 2 to stage 3) result from the complex stress pattern produced by the circular overpressure, and was achieved thanks to an uncommonly high numerical mesh resolution. I am not aware of previously published numerical studies that demonstrate such shear band geometries.

When gravity is neglected (or when lithostatic fluid pressures are present), the geometry of the modeled shear bands is similar to slip-line solutions predicted by circular plane strain indentation and display logarithmic eccentricity (Nadai, 1950; **Fig 3a**). When gravity is accounted for, numerical results show strong similarities with slip-line characteristics around a collapsing tunnel by d'Escatha and Mandel (1974, **Fig. 3c**).

An interesting comparison with flat indentation can also be made. Salençon (1969) showed that the maximum distance  $d_m=OJ$  from the indenter, at which slip-lines would cross each other along the central axis of symmetry before reaching the opposite free surface, satisfies a maximum height to width ratio  $d_m/a = 5.298$  ( $a$  is the half width of the indenter,  $J$  is slip-line intersection point beyond which triangular block motion links with opposite surface, **Fig 3b**). Such a local zone of dilation due to crossing shear zones has previously been applied in the field of Earth Sciences in order to explain the development of tensile structures

in compressional tectonic regimes. For instance Lake Baikal results from the indentation of Asia by India (e.g. Tapponnier & Molnar, 1976), and the Eifel volcanic zone would result from the Alpine-European indentation (Regenauer & Petit, 1997). Salençon's relationship ( $H > 5.3 R$  approximately) may be invoked to a first order to assess whether a magmatic chamber is deep enough to generate a secondary magmatic reservoir very close to the surface. This speculative process requires a systematic investigation of double sources below volcanoes worldwide (e.g. below Askja, Sturkell et al., 2006; below la Soufrière, Foroozan et al., 2010; and below Tungurahua, Ruiz et al., AGU Meeting of the Americas, Foz do Iguassu, 2010).

Structurally, the present modeled shear band structures dip inward when initiating from the ground surface, and dip outwards when initiating from the chamber wall. Despite the similarity, these geometrical results remain difficult to compare with numerical and analog studies that consider deflation instead of inflation (e.g. Kusumoto & Takemura, 2003; Acocella et al., 2004; Acocella 2007; Roche et al., 2001). **Fig. 8** schematizes our modeled geometries and relates them to structures likely observable in the field, with different depths corresponding to different levels of surface erosion and exhumation. Different imbricated structures appear: at the surface and possibly coeval with tensile cracks, normal faults form cones imbricated one into the other downwards, whereas close to the chamber reverse faults develop like imbricated flower pots. At intermediate depth, upward open cones and previous imbricated cones may coexist simultaneously, and overlap as deformation progresses. Such geometries should best be found on field in relatively old and well preserved plutonic and annular intrusive complexes, for which relatively slow ascent and cooling would maintain the structures deforming around them (e.g. Maza et al., 1998; Lafrance et al., 2001, Woodcock & Underhill, 1987). Clearly, a thorough investigation of natural analogues is needed to demonstrate the validity of these structural geometries.

## Conclusion

In studying the stress conditions for failure around a spherical magma chamber subjected to an internal overpressure, assuming an elasto-plastic bedrock and a simple approximation of fluid pore pressure, I have demonstrated the following points:

(a) Failure occurs in shear mode along the chamber walls, and for an internal overpressure (in excess of the state of lithostatic equilibrium) about half an order of magnitude (depending on the radius-to-depth ratio) greater than the usually inferred limit given by rocks tensile strength. Thus the important role of the wall-parallel component of the lithostatic stress on failure conditions (Grosfils, 2007) is confirmed. I also show that a chamber wall should fail in shear mode rather than in tensile mode, a common behavior also assumed in tunneling engineering mechanics (e.g. Massinas & Sakellariou, 2009).

(b) Only in the specific case where the bedrock is at a state of lithostatic pore fluid pressure does tensile failure occur around the chamber for an internal overpressure close to the tensile strength (5-10 MPa). Consequently, if the bedrock surrounding an active volcano contains less than lithostatic pore fluid pressures, then geodetic studies that use the Mogi solutions to infer chamber depth and radius should not be surprised to achieve their data fit with associated « high » overpressures. In addition, ground surface deformation rapidly exceeds elastic solutions as soon as the failure domain connects the chamber to the surface.

(c) The exceptionally precise geometries of the modeled shear bands were obtained thanks to a high mesh resolution, and I make a call to the community to confirm these results with future benchmarks (Gerbault et al., in prep.). These high resolution shear bands are comparable to slip-line plasticity solutions in displaying eccentric structures, and suggest that an initially deep magmatic chamber may generate a secondary reservoir closer to the surface, at the locus of intersection of major shear zones along the vertical axis of symmetry.

Further systematic documentation of double reservoirs in magmatic systems is needed to confirm this scenario.

Naturally, all these results are valid in the context of an ideally circular magmatic chamber in a homogeneous, isotropic, elasto-plastic medium. A finger- or dyke-shaped intrusion would in turn, be better modeled with the crack theory sensitive to the host rock tensile strength. As mentioned by Marti et al. (2008) or modeled by McLeod and Tait (1999), dyke intrusion may significantly affect the conditions for fault nucleation and propagation, therefore the applicability of our model results is obviously limited to the circular geometry of the chamber. In addition, deformation is also governed by the rheology of the magma, temperature and viscosity of the bedrock, the driving pressure, stresses resulting from the intrusion itself, dynamic fluid transport through the chamber and the bedrock, and many other temporally and spatially variable factors discussed elsewhere in the literature (e.g. Anderson, 1936; Rubin and Pollard, 1987; Lister and Kerr, 1991; Rubin, 1995; Day, 1996; Fialko et al., 2001; Hurwitz et al., 2009; Karlstrom et al., 2010, Galgana et al., 2011, de Saint Blanquat et al., 2011). Our near future perspectives are to improve the modeling of coupled hydromechanics (Gerbault et al., in prep.), study deflating conditions, and adapt these models to real volcanoes.

*Acknowledgements:* M.G. thanks R. Hassani, J. Salençon, M. Sakellariou for sharing their knowledge on mechanics, and O. Roche, V. Cayol, D. Healy, S. Holford, B. Mercier Lepinay, R. Plateaux, C. Ganino, for sharing their knowledge on magmatic chambers. Jelena Giannetti provided priceless library support, and J. Trevisan helped with the drawings. Nolwenn Croiset co-explored preliminary models with M.G., and her work is acknowledged (Masters report, ENS Lyon, 2007). A detailed and enriching review by Eric Grosfils improved the manuscript significantly.

## References

- Acocella, V., Funicello, R., Marotta, E., Orsi, G., deVita, S., 2004. The role of extensional structures on experimental calderas and resurgence. *Journal of volcanology and Geothermal Research* **129**, 199-217.
- Acocella, V., Understanding caldera structure and development: An overview of analogue models compared to natural calderas. *Earth Sciences Reviews* **85**, 125-160, 2007.
- Anderson, E.M., 1936. The dynamics of formation of cone-sheets, ring-dykes and cauldron-subsidences. Proceedings of the Royal Society, Edinburgh 56, 128–163.
- Bonafede, M., Dragoni, M., Quarenì, F., 1986. Displacement and stress fields produced by a centre of dilation and by a pressure source in a viscoelastic half-space: application to the study of ground deformation and seismic activity at Campi Flegrei, Italy. *Geophysical. Journal of the Royal Astronomy Society* **87**, 455–485.
- Bonafede, M., Ferrari, C., 2009. Analytical models of deformation and residual gravity changes due to a Mogi source in a viscoelastic medium. *Tectonophysics* **471**, 4-13.
- Bower S.M., Woods A.W., 1997, control of magma volatile content and chamber depth on the mass erupted during explosive volcanic eruptions, *Journal of Geophysical Research* **102**, 10273-10290.
- Burov, E., Guillou-Frottier, L., 1999. Thermomechanical behavior of large ash flow calderas, *Journal of Geophysical Research* **104**, 23081-23109.
- Burov, E., Jaupart, C., Guillou-Frottier, L., 2003. Ascent and emplacement of buoyant magma bodies in brittle-ductile upper crust. *Journal of Geophysical Research* **108**, 2177.
- Caquot A., Kerisel J., 1956. *Traité de Mécanique des Sols*, Gauthier-Villars (eds), Paris.
- Chery, J., Bonneville, A., Villote, J.P., Yuen, D., 1991. Numerical modeling of caldera dynamical behaviour, *Geophysical Journal International* **105**, 365-379.
- Chery, J., Zoback, M.D. & Hassani, R., 2001. An integrated mechanical model of the San Andreas Fault in central and northern California. *Journal of Geophysical Research* **106**, 22 051–22 066.
- Cundall, P., Board, M., 1988. A microcomputer program for modeling large-strain plasticity problems. *Numerical Methods in Geomechanics* **6**, 2101–2108.
- Cundall, P.A., 1989. Numerical experiments on localization in frictional materials. *Ingenior Archives* **59**,148–159.
- Day S.J.,1996. Hydrothermal pore fluid pressure and the stability of porous, permeable volcanoes. *In: McGuire W.J. Jones A.P. Neuber J. (eds) Volcano stability on the Eath and other planets*, Geological Society, London, Special Publications **110**, 77-93.
- D'Escatha Y., Mandel J., 1974, Stabilité d'une galerie peu profonde en terrain meuble, *Industrie Minerale*, Numero Special, 45-53.
- Ellis, S.M., Wilson, C.J.N., Bannister, S., Bibby, H.M., Heise, W., Wallace, L., Patterson, N., 2007. A future magma inflation event under the rhyolitic Taupo volcano, New Zealand: Numerical models based on constraints from geochemical, geological and geophysical data. *Journal of volcanology and Geothermal Research* **168**, 1-27.
- Engelder, T., Leftwich, J.T., 1997. A pore-pressure limit in overpressured South Texas oil and gas field, *In: R.C. Surdam, (eds) Seals, traps, and the petroleum system*, AAPG Memoir 67, Chapter

- Foroozan R., Elsworth D., Voight B., Mattioli G.S., 2010. Dual reservoir structure at Soufrière Hills volcano inferred from continuous GPS observations and heterogeneous elastic modeling, *Geophysical Research Letters* **37**, doi:10.1029/2010GL042511.
- Fairhurst C., Carranza-Torres C., 2002. Closing the circle, some comments on design procedures for tunnel supports in rock. In: J.F. Labuz & Bentler J.G. (eds) *Proceedings, University of Minnesota 50<sup>th</sup> Annual Geotechnical Conference*, Minneapolis University Minnesota, 21-84.
- Fialko, Y., Khazan, Y., Simons, M., 2001. Deformation due to a pressurized horizontal circular crack in an elastic half-space, with applications to volcano geodesy. *Geophysical Journal International* **146**, 181-190.
- Galgana, G. A., P. J. McGovern, E. B. Grosfils, 2011. Evolution of large Venusian volcanoes: Insights from coupled models of lithospheric flexure and magma reservoir pressurization, *Journal of Geophysical Research*, doi:10.1029/2010JE003654.
- Gerbault, M., Poliakov, A., Daignières, M., 1998. Prediction of faulting from the theories of elasticity and plasticity : what are the limits ? *Journal of Structural Geology* **20**, 301-320.
- Geyer, A., Marti J., 2009. Stress fields controlling the formation of nested and overlapping calderas: Implications for the understanding of caldera unrest. *Journal of Volcanology and Geothermal Research* **181**, 185-195.
- Gray, J.P., Monaghan, J.J., 2004. Numerical modeling of stress fields and fracture around magma chambers , *Journal of Volcanology and Geothermal Research* **135**, 259-283.
- Gressier J-B., Mourgues R., Bodet L., Matthieu J-Y., Galland O., Cobbold P., 2010. Control of pore fluid pressure on depth of emplacement of magmatic sills: an experimental approach, *Tectonophysics* **489**, 1-12.
- Grosfils, E.B., 2007. Magma reservoir failure on the terrestrial planets: assessing the importance of gravitational loading in simple elastic models. *Journal of Volcanology and Geothermal Research* **166**, 47–75.
- Gudmundsson, A., 1988. Effect of tensile stress concentration around magma chambers on intrusion and extrusion frequencies. *Journal of volcanology and Geothermal Research* **35**, 179-194.
- Gudmundsson, A., J. Marif, E. Turon, 1997. Stress field generating ring faults in volcanoes *Geophysical Research Letters* **24**, 1559-1562.
- Gudmundsson, A., Fjeldskaar, I., Brenner, S.L., 2002. Propagation pathways and fluid transport of hydrofractures in jointed and layered rocks in geothermal fields. *Journal of Volcanology and Geothermal Research* **116**, 257–278.
- Gudmundsson, A., 2006. How local stresses control magma-chamber ruptures, dyke injections, and eruptions in composite volcanoes, *Earth-Science Reviews* **79**, 1-31.
- Guillou-Frottier, L., Burov, E.B., Milesi, J.P., 2000. Genetic links between ash flow calderas and associated ore deposits as revealed by large-scale thermo-mechanical modeling, *Journal of volcanology and Geothermal Research* **102**, 339–361.
- Hardy, S., 2008. Structural evolution of calderas: insights from two-dimensional discrete element formulations? *Geology* **36**, 927-930.
- Hassani, R., D. Jongmans, J. Chéry, 1997. *Study of plate deformation and stress in subduction processes using two-dimensional numerical models*. *Journal of Geophysical Research* **102**, 17951-17965.

- Henry C.D., Kunk M.J., Muehlberger W.R., McIntosh W.C., 1997. Igneous evolution of a complex laccolith-caldera, the Solitario, Trans-Pecos Texas: Implications for calderas and subjacent plutons, *Geological Society of America Bulletin* **10**, 1036–1054.
- Hillis, R.R., 2003. *Pore pressure/stress coupling and its implications for rock failure*. Geological Society, London, Special Publications **216**, 359-368, doi :10.1144/GSL.SP.2003.216.01.23
- Hubbert, M.K., W.W. Rubey, 1959. Role of fluid pressure in mechanics of overthrust faulting. *Geological Society of America Bulletin* **70**, 115–166.
- Holohan P., Troll V.R., Errington M., Donaldson C.H., Nicoll G.R., Emeleus C.H., 2009. *Geological Magazine* **146**, 400 - 418.
- Huppert, H., Woods A.W., 2002. The role of volatiles in magma chamber dynamics, *Nature* **420**, 493–495.
- Itasca Consulting Group, 2006. FLAC<sup>3D</sup>, *Fast Lagrangian Analysis of Continua in 3 Dimensions. Version 3.0*. Minnesota: Itasca Consulting Group, Minneapolis.
- Hurwitz D.H., Long S.M., Grosfils E.B., 2009. The characteristics of magma reservoir failure beneath a volcanic edifice, *Journal of Volcanology and Geothermal Research* **188**, 379-394, DOI: 10.1016/j.jvolgeores.2009.10.004.
- Jeffery, J.B., 1920. Plane stress and plane strain in bi-polar coordinates. *Transactions of the Royal Society, London* **221**, 265–293.
- Johnson D.J., Sigmundsson F., Delaney P.T., 2000. Comment on “volume of magma accumulation or withdrawal estimated from surface uplift or subsidence, with application to the 1960 collapse of Kilauea volcano”, Delaney & McTigue (eds) *Bulletin of Volcanology* **61**, 491-493.
- Karlstrom, L., Dufek J., Manga M., 2010. Magma chamber stability in arc and continental crust, *Journal of Volcanology and Geothermal Research*, doi: 10.1016/j.jvolgeores.2009.10.003
- Kaus B., 2010. Factors that control the angle of shear bands in geodynamic numerical models of brittle deformation , *Tectonophysics* , 36-47.
- Kusumoto, S., Takemura, K., 2003. Numerical simulation of caldera formation due to collapse of a magma chamber, *Geophysical Research Letters* **30**, doi:10.1029/2003GL018380.
- Lafrance, B., John, B.E., 2001. Sheeting and dyking emplacement of the Gunnison annular complex, SW Colorado, *Journal of Structural Geology* **23**, 1141-1150.
- Lavier L., Buck W., Poliakov A., 2000. Factors controlling normal fault offset in an ideal brittle layer, *Journal of Geophysical Research* **105**, 23431-23442.
- Lister, J.R., Kerr, R.C., 1991. Fluid-mechanical models of crack propagation and their application to magma transport in dykes. *Journal of Geophysical Research* **96** :10049–10077.
- Marti, J., Geyer, A., Folch, A., Gottsmann J., 2008. A review of collapse caldera modeling. *In: Developments in Volcanology* **10**, DOI 10.1016/S1871-644X(07)00006-X, 233-283.
- Masek, J.G., Duncan, C.C., 1998. Minimum-work mountain building, *Journal of Geophysical Research* **103**, 907-917.
- Masterlark, T., Z. Lu, 2004. Transient volcano deformation sources imaged with interferometric synthetic aperture radar: Application to Seguam Island, Alaska. *Journal of Geophysical Research* **109**, doi:10.1029/2003JB002568.
- Masterlark, T., 2007. Magma intrusion and deformation predictions: Sensitivities to the Mogi assumptions. *Journal of Geophysical Research* **112**, doi:10.1029/2006JB004860.

- Massinas, S.A., Sakellariou, M.G., 2009. Closed-form solution for a plastic zone formation around a circular tunnel in half-space obeying Mohr-Coulomb criterion. *Géotechnique* **59**, 691-701, doi: 10.1680/geot8.069.
- Maza, M., Briquieu, L., Dautria, J-M., Bosch, D., 1998. Le complexe annulaire d'âge Oligocène de l'Achkal (Hoggar Central, Sud Algérie): témoin de la transition au Cénozoïque entre les magmatismes tholéitique et alcalin. Evidences par les isotopes du Sr, Nd, Pb, *Geochemistry. Academie des Sciences, Elsevier, Paris*. 167-172.
- McLeod, P., Tait, S., 1999. The growth of dyke from magma chambers. *Journal of volcanology and Geothermal Research* **92**, 231–245.
- McTigue, D.F., 1987. Elastic stress and deformation near a finite spherical magma body: resolution of a point source paradox. *Journal of Geophysical Research* **92**, 12931–12940.
- Mogi K., 1958. Relations between the eruption of various volcanoes and the deformation of the ground surfaces around them. *Bulletin of the Earthquake Research Institute*, **36** :99–134.
- Nadai A., 1950. *The theory of flow and fracture of solids*. Mc-Graw-Hill, New York. 402 p.
- Pinel, V., Jaupart, C., 2003. Magma chamber behavior beneath a volcanic edifice. *Journal of Geophysical Research* **108**, doi:10.1029/2002JB001751.
- Pinel, V., Jaupart, C., 2005. Caldera formation by magma withdrawal from a reservoir beneath a volcanic edifice. *Earth and Planetary Science Letters* **230**, 273–287.
- Poliakov, A., Podladchikov, Y., 1992. Diapirism and topography. *Geophysical Journal International* **109**, 553–564.
- Podladchikov Y., Poliakov A., Cundall P., 1993. An explicit inertial method for the simulation of visco-elastic flow: an evaluation of elastic effects on diapiric flow. *Flow and creep in the solar system: observation, modeling and theory* **391**, 175–195.
- Pritchard, M.E., M. Simons, 2004. An insar-based survey of volcanic deformation in central Andes, *Geochemistry Geophysics Geosystems* **5**, doi:10.1029/2003GC000610.
- Ramsey J.M., Chester F.M., 2004. Hybrid fracture and the transition from extension fracture to shear fracture. *Nature* **428**, 63-66.
- Regenauer-Lieb K., Petit J.P., 1997. Cutting of the European continental lithosphere: plasticity theory applied to the Alpine collision. *Journal of Geophysical Research* **102**, 7731-7746.
- Reid, M.E., 2004. Massive collapse of volcano edifices triggered by hydrothermal pressurization. *Geology* **32**, 373-376.
- Rivalta, E., Segall P., 2008. Magma compressibility and the missing source for some dike intrusions. *Geophysical Research Letters* **35**, L04306, doi:10.1029/2007GL032521.
- Roche, O., Druitt T.H., 2001. Onset of caldera collapse during ignimbrite eruptions, *Earth and Planetary Science Letters* **191**, 191-202.
- Rubin, A.M., Pollard, D.D., 1987. Origins of blade-like dikes in volcanic rift zones. *U.S. Geological Survey Professional Paper* **1350**, 1449–1470
- Rubin, A.M., 1995. Propagation of magma-filled cracks. *Annual Review, Earth and Planetary Sciences* **23**, 287–336.
- de Saint Blanquat M., Horsman E., Habert G., Morgan S., Vanderhaeghe O., Law R., Tikoff B., 2011. Multiscale magmatic cyclicity, duration of pluton construction, and the paradoxical relationship

- between tectonism and plutonism in continental arcs, *Tectonophysics* **500**, 20-33.
- Salençon, J., 1966. Expansion quasi-statique d'une cavité à symétrie sphérique ou cylindrique dans un milieu élastoplastique. *Annales des Ponts et Chaussées* **III**, 175-187.
- Salençon, J., 1969. *La théorie des charges limites dans la résolution des problèmes de plasticité en déformation plane*. Thèse de Doctorat ès sciences, Paris, 124 p.
- Sartoris G., Pozzi J.P., Philippe C., le Mouel J.L., 1990. Mechanical instability of shallow magma chambers. *Journal of Geophysical Research* **95**, 5141-5151.
- Segall, P., 2009. Earthquake and volcano deformation. Princeton University Press. p. 432.
- Sturkell E., Sigmundsson F., Slunga R., 2006. 1983–2003 decaying rate of deflation at Askja caldera: Pressure decrease in an extensive magma plumbing system at a spreading plate boundary, *Bulletin of Volcanology* **68**, 727–735, DOI 10.1007/s00445-005-0046-1.
- Tait S., Jaupart C., Vergnolle S., 1989. Pressure, gas content and eruption periodicity of a shallow, crystallizing magma chamber. *Earth and Planetary Science Letters* **92**, 107–123.
- Tapponnier P., Molnar P., 1976. Slip-line field theory and large-scale continental tectonics. *Nature* **264**, 319-324.
- Timoshenko S., Goodier J.N., 1970. *Theory of Elasticity*, McGraw-Hill Higher education 2<sup>nd</sup> edition, 608 p.
- Townend J., Zoback M.D., 2000. How faulting keeps the crust strong, *Geology* **28**, 399-402.
- Trasatti E. Giunchi C., Bonafede M., 2005. Structural and rheological constraints on source depth and overpressure estimates at the Campi flegrei caldera, Italy, *Journal of Volcanology and Geothermal Research* **144**, 105-118.
- Vermeer P.A., de Borst R., 1984. Non-associated plasticity for soils, concrete and rocks. *Heron* **29**, 1–75. Stevin-Laboratory of Civil Engineering, University of Technology, Delft, and Institute TNO for Building Materials and Building Structures, Rijswijk, The Netherlands.
- Verruijt A., 1998. Deformations of an elastic half plane with a circular cavity, *International Journal of Solids Structures* **35**, 2795-2804.
- Waite G.P., Smith R.B., 2002. Seismic evidence for fluid migration accompanying subsidence of the Yellowstone caldera. *Journal of Geophysical Research* **107**, doi:10.1029/2001JB000586.
- Wegler U., Lühr B-G., Snieder R., Ratdomopurbo A., Increase of shear wave velocity before the 1998 eruption of Merapi volcano (Indonesia). *Geophysical Research Letters* **333**, doi:10.1029/2006GL025928,2006.
- White, B.G., Larson M.K., Iverson S.R., 2004. Origin of mining-induced fractures through macro-scale distortion. In: Gulf Rocks 2004. In: *Rock Mechanics Across Borders and Disciplines, Proceedings of the Sixth North American Rock Mechanics Conference*, Houston, Texas. Report ARMA/NARMS **04-569**.
- Woodcock N.H., Underhill J.R., 1987. Emplacement-related fault patterns around the Northern granite, Arran, Scotland. *Geological Society of America Bulletin* **98**,515-527.
- Yarushina V.M., Dabrowski M., Podladchikov Y.Y., 2010. An analytical benchmark with combined pressure and shear loading for elastoplastic numerical models. *Geochemistry Geophysics Geosystems* **11**, doi:10.1029/2010GC003130.
- Zoback, M.D., 2007. *Reservoir geomechanics*. Cambridge University Press, 449 p.

**Table 1:** Description of parameters, and specific value given for the reference model only.

Symbol	Description	Value
R	Radius of chamber	2 km
H	Depth to center of chamber	7 km
D	Depth to crest of chamber, used by Grosfils(2009), H-R	5 km
G	Shear modulus: bedrock, chamber	20 GPa, 2 GPa
$\nu$	Poisson's ratio	0.25
$\rho$	density	2500 kg/m <sup>3</sup>
g	gravity	9.81 m <sup>2</sup> /s
$\alpha$	Angle between vertical axis and line at surface origin to any point at wall, used by Jefferys (1920)	
$\theta$	Angle between horizontal axis at chamber's center and any point at wall, used by Grosfils (2007)	
$\sigma_{xx}$	Horizontal stress	
$\sigma_{\theta\theta}$	Hoop stress at the chamber wall	
C	Free surface factor : $1+2\tan \alpha''$ , used by Grosfils(2007)	
$\varphi, \phi$	Bedrock friction angle	30°
$S_o$	Bedrock cohesion	10 MPa
$T_o$	Bedrock tension deduced from $S_o$	17.3 MPa
T	Bedrock cutoff tensile strength	5 MPa
P, $\sigma_{II}$	First and Second stress invariants	
$\tau, \sigma_n$	Tangential and normal stress along any given plane	
$\Delta P$	Internal overpressure	
$\Delta P_S$	Critical overpressure for tensile failure at the surface	Eq. 4
$\Delta P_T$	Critical overpressure for tensile failure predicted from common studies, neglecting gravity	Eq. 5
$\Delta P_{TG}$	Critical overpressure for tensile failure predicted by Grosfils (2007)	Eq. 7
$\Delta P_{MC}, \Delta P_{MCS}$	Critical overpressure for shear failure predicted in this study	Eq. 11, 12
$P_o, P_{cr}$	Uniform external pressure, and critical internal overpressure defined by Massinas & Sakellariou (2009)	Eq. 13
$\Delta P_1, \Delta P_2, \Delta P_3$	Modeled Internal overpressure at different stages of failure	
$\lambda$	Pore pressure ratio	0/1
$p_f$	Pore fluid pressure	

**Table 2:** Numerical Models. Initial conditions are distinguished according to the magmatic chamber being included or not in the mesh, fluid pore-pressure (hydrostatic or lithostatic), tensile strength T (elastic means the entire bedrock is elastic as opposed to elasto-plastic), and applied overpressure  $\Delta P$ . Results are summarised in terms of stage of fracturing and amount of surface uplift. Models in grey are displayed in the supplementary material (appendix).

Model name	process name	Fig.	chamber	Fluid pressure	T (MPa)	Pressure $\Delta P$ (MPa)	Fracturing stage	Surface uplift
<b>M1</b>	M3dp5b	4a	$\lambda=\mu=1$ GP A	-	5	54	1-surface	1.5 m
		4b				114	2-wall	4.1 m
		4c				127	3-connection	5.5 m
		4d				135	3-connection	6.7 m
<b>M2</b>	M3dp5L1	6a	$\lambda=\mu=1$ GP A	Hydrost	5	55	2-wall	1.5 m
<b>M3</b>	M3dp3L3	6b	$\lambda=\mu=1$ GP A	Lithost	5	20	2-wall	0.5 m
<b>M4</b>	M3dpR3L3a	6c	$\lambda=\mu=1$ GP A	Lithost	17.3	20	3-connection	1.0 m
<b>A1a</b>	M3f50r3	A1	$\lambda=\mu=1$ GPA	-	17.3	50	1-surface	2.06 m
<b>A1b</b>	M3cp50elas	A1	$\lambda=\mu=1$ GPA	-	elastic	50	elastic	2.05 m
<b>A1c</b>	bull9	A1	empty	-	17.3	50	1-surface	2.13 m
<b>A1d</b>	bull9elas	A1	empty	-	elastic	50	elastic	2.13 m
<b>A2a</b>	M3cp120	A2	$\lambda=\mu=1$ GPA	-	17.3	120	2-wall	4.9 m
<b>A2b</b>	M3cp120elas	A2	$\lambda=\mu=1$ GPA	-	elastic	120	2-wall	5.11 m
<b>A2c</b>	bull9	A2	empty	-	17.3	120	2-wall	5.12 m
<b>A2d</b>	bull9elas	A2	empty	-	elastic	120	2-wall	5.25 m
<b>A3a</b>	M3cp20nog	A3	$\lambda=\mu=1$ GPA	-	17.3	15.2	2-wall	1.08 m
<b>A3b</b>	bull9nog	A3	empty	-	17.3	15.2	2-wall	1.18 m
<b>A3c</b>	M3dpcL3	A3	$\lambda=\mu=1$ GPA	Lithost	17.3	18.1	2-wall	1.15 m
<b>A3d</b>	bull8nog	A3	empty	-	17.3	18.8	2-wall	2.5 m

## Figure Captions

Fig. 1. Parametric definition of the problem. Grey values are those defined by Grosfils (2007).

Fig. 2. Pressure difference  $\Delta P$  required to initiate failure at the chamber wall, according to different assumptions: tensile failure accounting for free-surface without gravity ( $\Delta P_T$ , Eq. 5), and with gravity (Grosfils, 2007;  $\Delta P_{TG}$ , Eq. 9), and Mohr-Coulomb shear failure with and without a free-surface ( $\Delta P_{MC}$ , Eq. 11, and  $\Delta P_{MCS}$ , Eq. 12). Here both depth and overpressure are taken positive. Failure onset is predicted where the critical overpressure is minimal: it initiates at the crest when  $H=7$  km and  $R=2$  km (depth  $h=0$  and angle  $\theta=90^\circ$ ), and at  $h\sim 0.2$  km when  $H=2$  km and  $R=1$  km.

Fig. 3. Solutions from engineering mechanics. (a) Slip-line solution for circular indentation in a perfectly plastic infinite medium (after Nadai, 1950, in which a photograph of steel indentation shows striking similarity). (b) Closed-form solution for flat indentation, displaying slip-line intersection at the axis of symmetry of flat indentation for  $OJ/a > 5.298$  (after Salençon, 1969). (c) Slip-line characteristics calculated by d'Escatha & Mandel (1974) for a friction angle  $\varphi=20^\circ$ . (d) Plasticized domain calculated by Massinas & Sakellariou (2009) for different internal support pressures ( $P_i$ ) in tunnels (note the 'ears' shape appearing at some stage).

Fig. 4. Reference model M1 for different stages of increasing internal pressure ( $\Delta P$ ), tensile strength  $T=5$  MPa. (a) Stage 1: tensile failure initiates at the surface when  $\Delta P_1=28$  MPa, later forming inward dipping normal faults. (b) Stage 2: Shear failure initiates around the chamber walls from  $\Delta P_2=70$  MPa, and forms an eccentric fault pattern here shown at  $\Delta P=100$  MPa. (c) Stage 3: Both fault systems connect, at  $\Delta P_3=130$  MPa. (d) The fault system expands, forming a vertical fault pattern from the chamber to the surface. Figures show, from left to right, rupture zones in blue, the 2<sup>nd</sup> invariant of the cumulated deviatoric shear strain, and the 2<sup>nd</sup> invariant of the stress tensor.

Fig. 5. Surface displacements from model M1 at different times T1, T2 and T3 corresponding to stages illustrated in Fig. 4. Vertical displacement is shown as a function of distance (left) and as a function of time (right). Note departure from linear increase at T3, when the failure pattern connects the chamber to the surface.

Fig. 6. Models accounting for an effective pore-fluid pressure in the host rock. (a) Hydrostatic pore pressure, tensile strength  $T = 5$  MPa, for  $\Delta P = 54$  MPa. Tensile failure develops at the top surface and shear failure occurs at the wall (dark blue dots). (b) Lithostatic pore pressure, tensile strength  $T = 5$  MPa, for  $\Delta P = 20$  MPa. Tensile failure develops all around the chamber wall. (c) Lithostatic pore pressure with no tensile strength cutoff ( $T = T_o = 17.3$  MPa), at  $\Delta P = 20$  MPa. Shear failure.

Fig. 7. Field examples of shear fractures around magmatic bodies. a) The Solitario laccolith, Texas, showing dyke intrusions bounded by pre-existing shear faults (simplified after Henry et al., 1997). (b) Geological structural map of Arran Island, Scotland, with interpreted map and plane views of structures forming during pluton ascent, after Woodcock & Underhill (1987). (c) Detail rock sampled at Arran Island in the Glen Rosa valley, displaying a conjugate fracture pattern along which fluid penetration occurs at location A, and a non-oriented more massive intrusion at location B.

Fig. 8. Diagram of failure patterns from the surface to the top of a circular pluton, displaying the imbrications of individual faulted blocks for different depths. A zone of dilation forms locally at the crossing point between upward- and downward propagating shear zones, suggesting the formation of a secondary magmatic reservoir (compare with Fig. 3b).

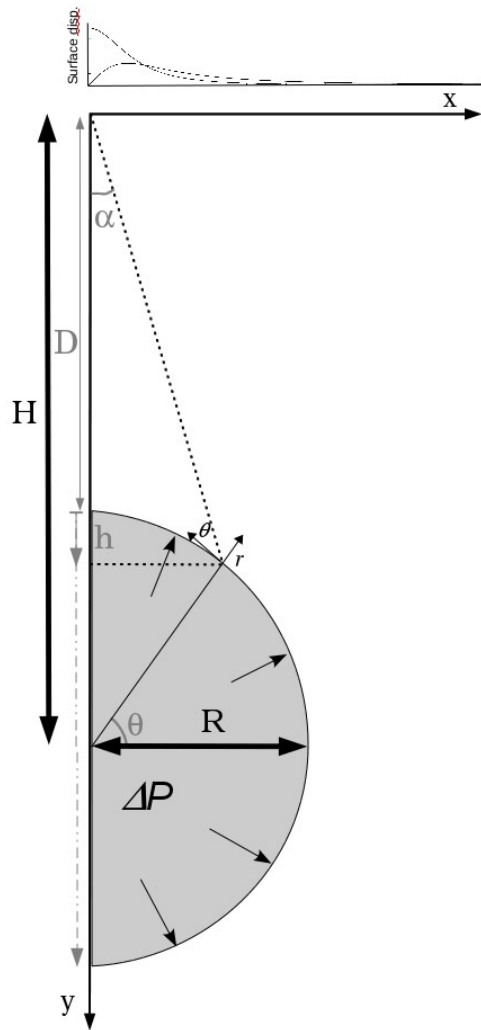


Figure 1 -Gerbault

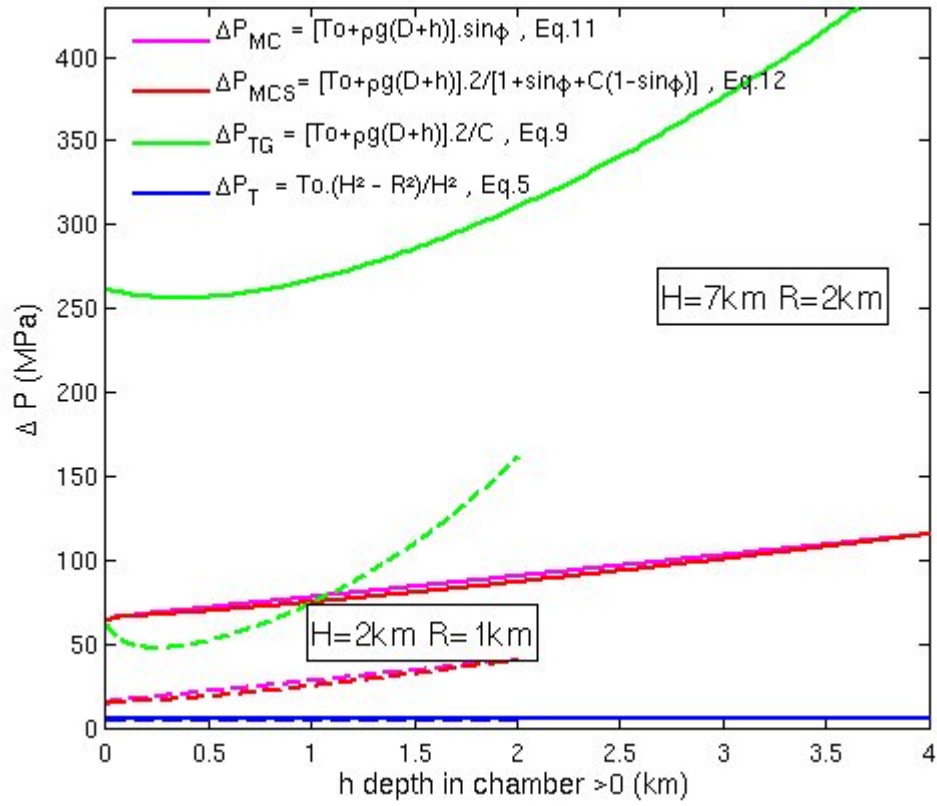


Figure 2 - Gerbault

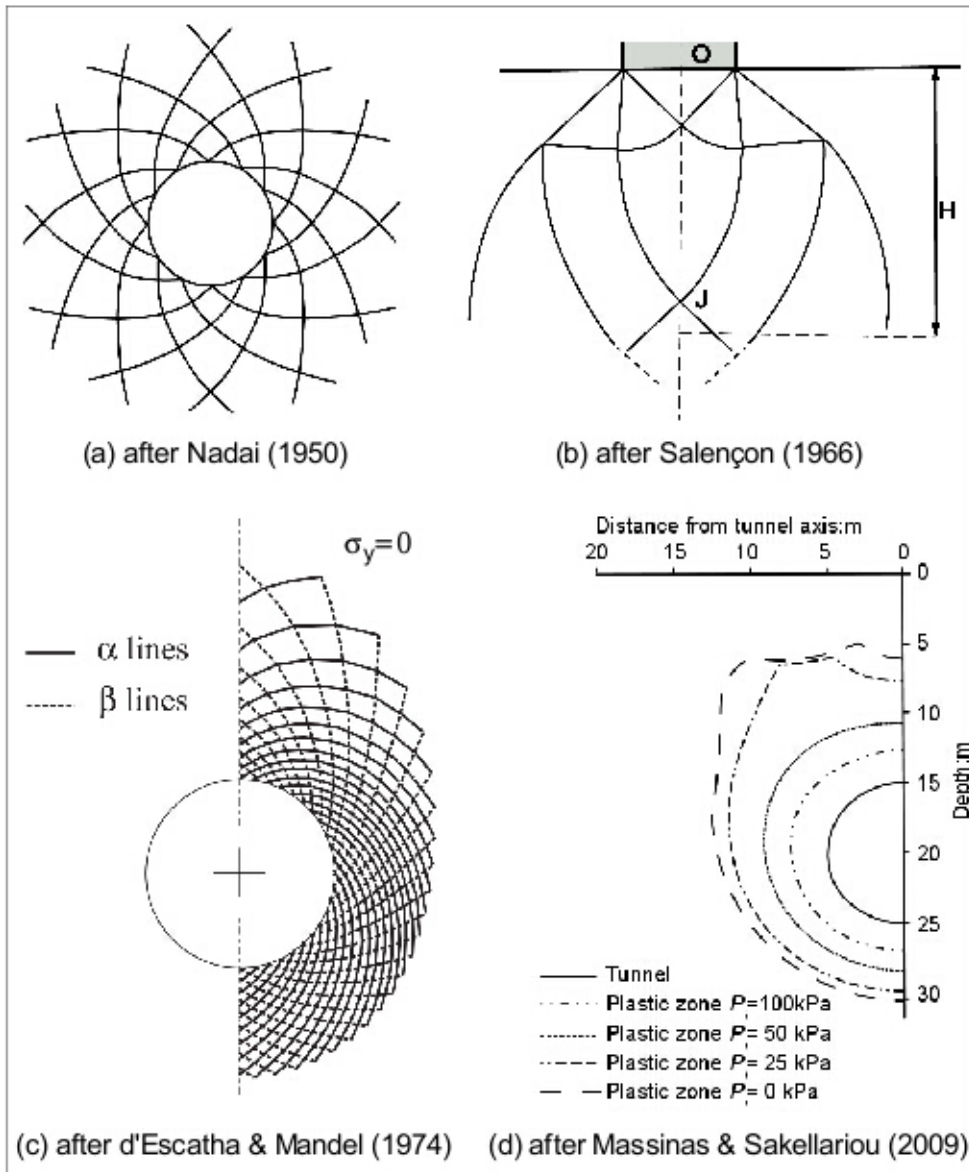


Figure 3- Gerbault

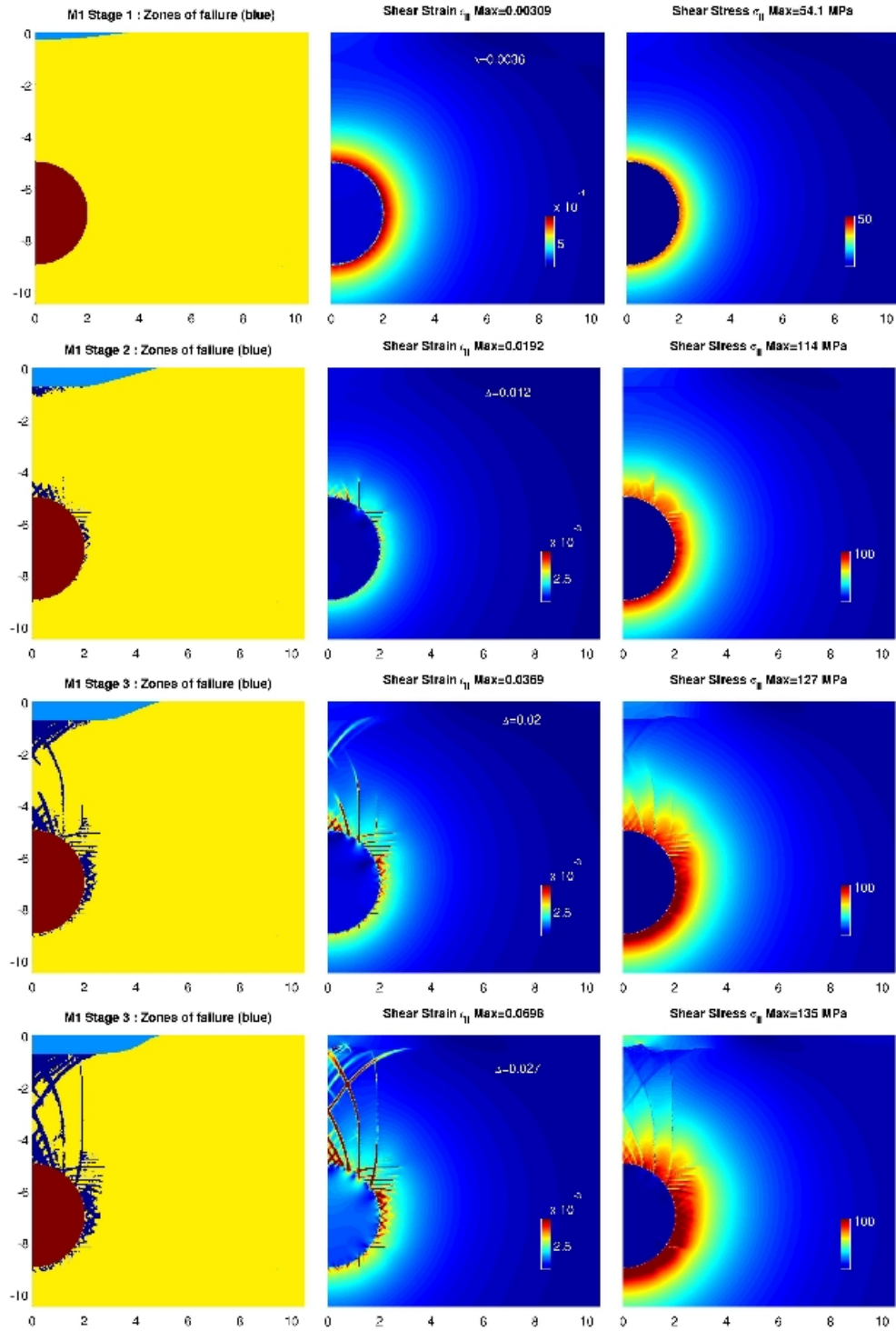


Figure 4 - Gerbault

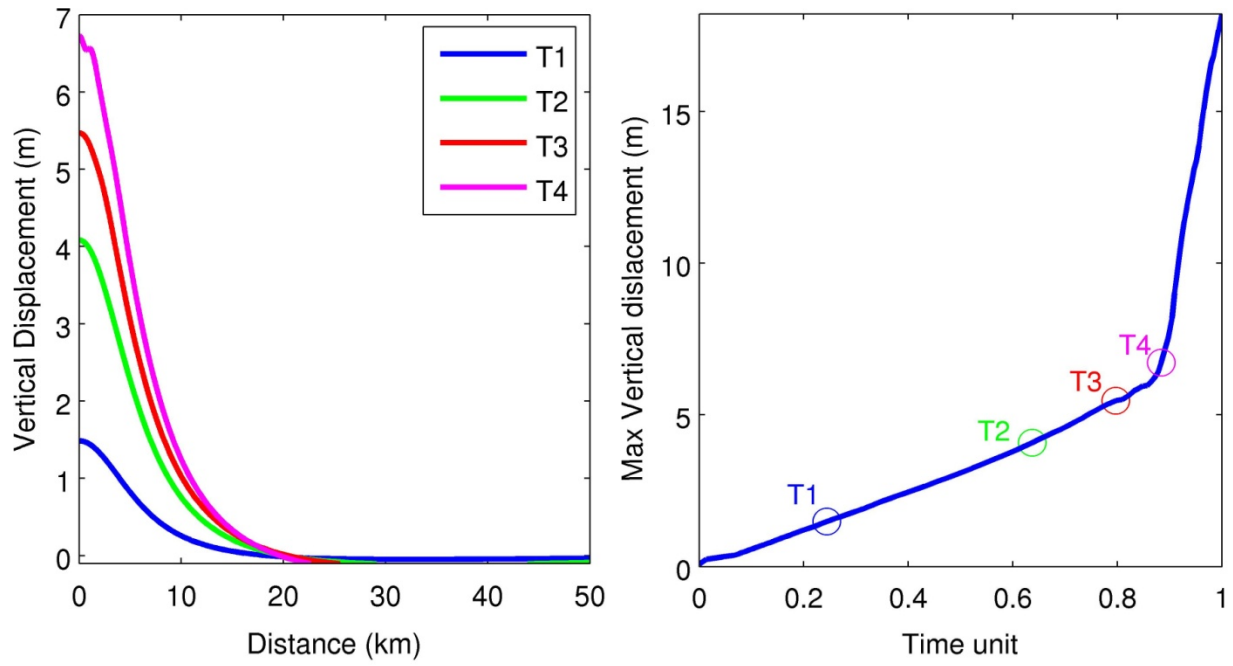


Figure 5 -Gerbault

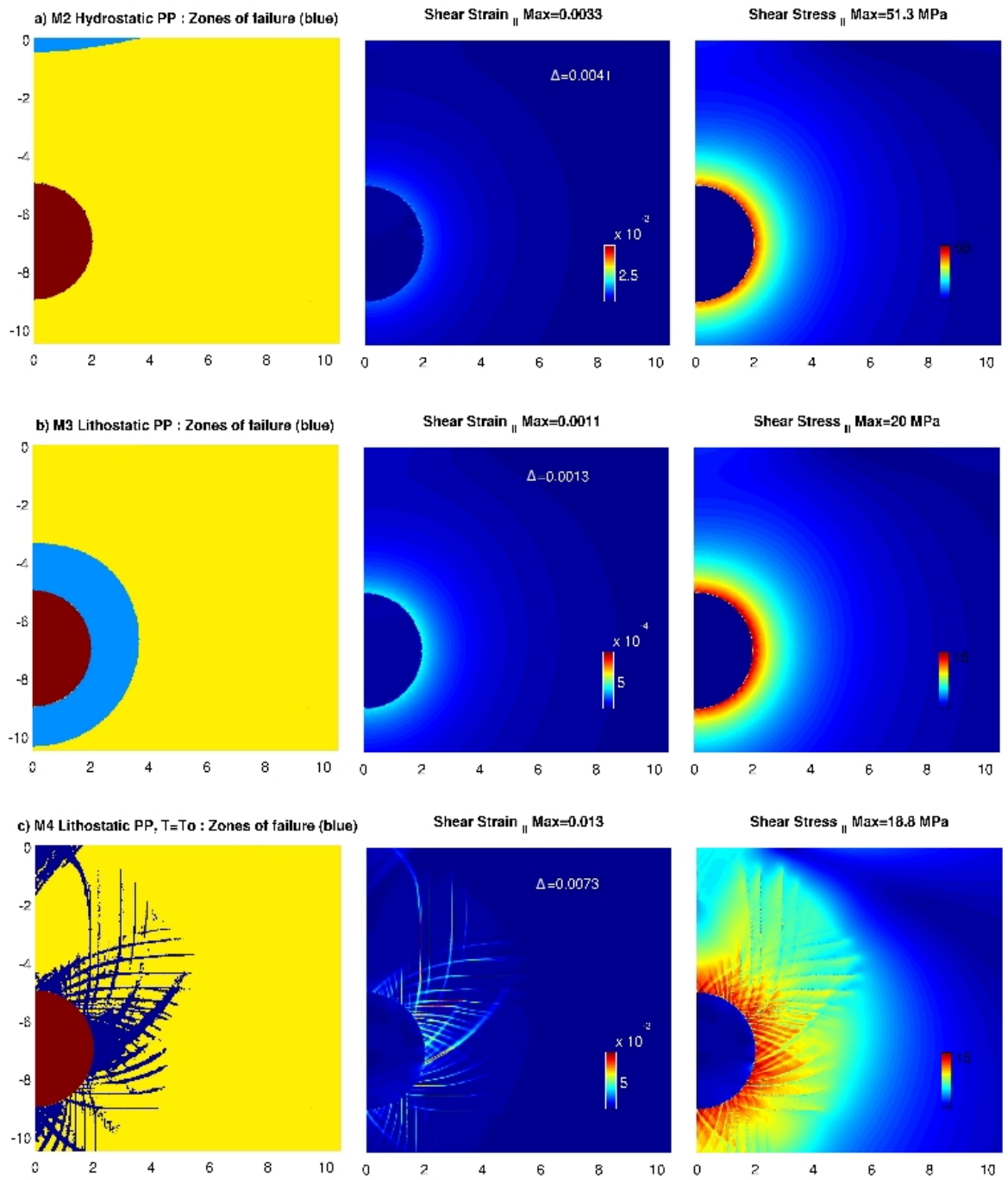


Figure 6 - Gerbault

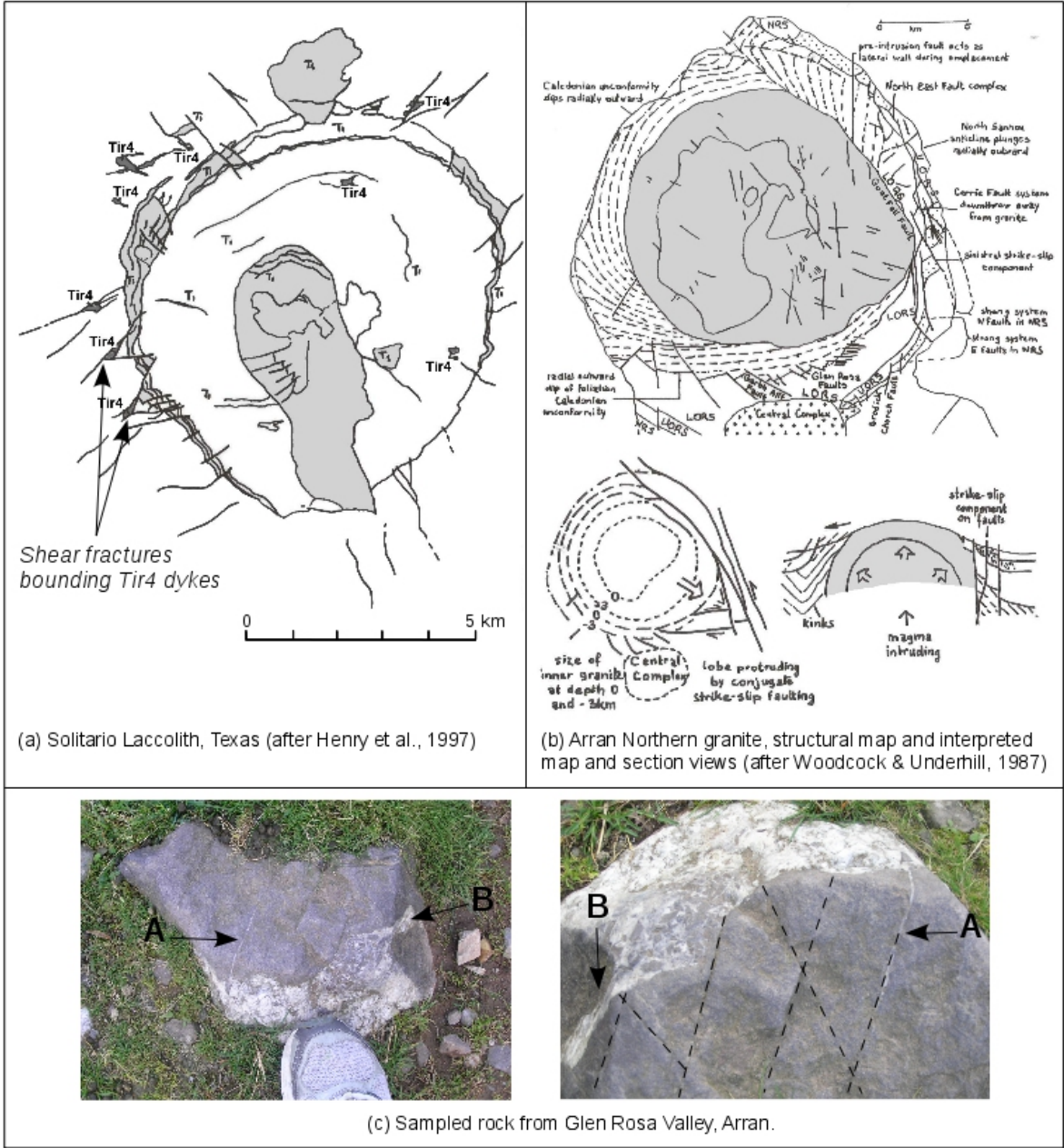


Fig. 7.

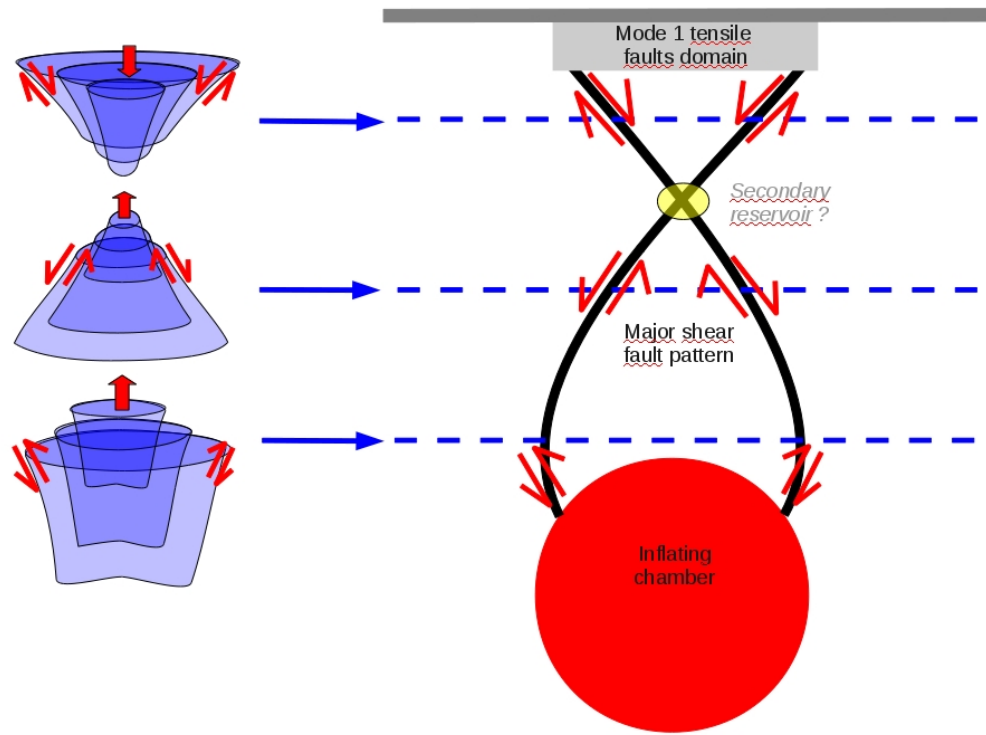


Figure 8 - Gerbault

**Supplementary material:** [Appendix, numerical benchmark] is available at [www.geolsoc.org.uk/SUP00000](http://www.geolsoc.org.uk/SUP00000)

The models presented in this paper use the finite-differences code Parovoz (Poliakov & Podladchikov, 1992; Podladchikov et al., 1993), which is based on the FLAC method (Cundall & Board, 1988), and builds a quadrilateral Lagrangian mesh. This condition requires to incorporate the chamber inside the mesh if one wishes to achieve a very high mesh resolution. Then, the elastic properties of the meshed chamber determine its capacity to dilate, and thus the amount of pressure transferred through its walls into the bedrock domain. Consequently, internal overpressure is best measured by the maximum deviatoric stress recorded at the modeled magmatic chamber walls (e.g. Chery et al., 1991), and is the value to compare with analytical predictions. Differences in modeled results are thus expected when compared to models with « empty chambers » meshes.

Here we benchmark our models with a finite element code, ADELI (Hassani et al., 1997; Chery et al., 2001), with triangular mesh elements and an explicit dynamic relaxation method similar to FLAC. The mesh can be defined radial about the chambers' circular boundary. Adeli has been widely applied to various geodynamical settings (e.g. [http://www.dstu.univ-montp2.fr/PERSO/chery/Adeli\\_web/doc/publis2007.htm](http://www.dstu.univ-montp2.fr/PERSO/chery/Adeli_web/doc/publis2007.htm)), and the method details can be found for example in Chery et al. (2001). Because of computational time issues, mesh resolution in Adeli is chosen of the order of 50 m at the chambers' wall, 2 times coarser than in Parovoz.

Plasticity in Adeli is accounted for slightly differently than in Parovoz. At failure, Parovoz employs the Mohr-Coulomb failure criterion by means of an explicit algorithm, whereas Adeli employs an implicit algorithm and the Drucker-Praeger yield criterion. Therefore, despite friction angle and cohesion being defined in Adeli to coincide with conventional Mohr-Coulomb values, slight differences still remain. In addition, Adeli does not include a tensile cutoff strength, but instead the default tensile strength deduced from cohesion  $T_0 = S_0 / \tan \phi$ . Therefore this value is also taken in Parovoz for the present benchmarks.

#### **A1) Benchmark under mostly elastic conditions, $\Delta P = 50 \text{ MPa}$**

Stress and strain at the surface obtained in our reference model (Fig. 4) are compared with those obtained with Adeli, at the specific internal overpressure  $\Delta P = 50 \text{ MPa}$ . At this stage, most of the domain is elastic, apart from a few hundred meters below the ground surface at origin  $X_0$ . 4 models are displayed, with purely elastic and elasto-plastic solutions for each code Parovoz and Adeli.

Fig. A1 from top to bottom, displays surface displacements and horizontal stress at the surface (top figures), and 2D contours of failure zones, shear-strain and shear-stress for Parovoz and for Adeli, in the middle and bottom of the figure, respectively.

Elastic solutions are nearly undistinguishable from elasto-plastic solutions for each code, except for the horizontal stress ( $\sigma_{xx}$ ) at the origin where failure has initiated: in this case  $\sigma_{xx}$  is limited by the rock tensile strength in Parovoz, whereas Adeli's failure criterion allows for a higher yield at the same location. Also, differences in mesh resolution lead to different averaged stress over an element thickness, therefore also, the occurrence of local differences. This explains why rock failure at the top surface has a slightly greater extent in Parovoz than in Adeli.

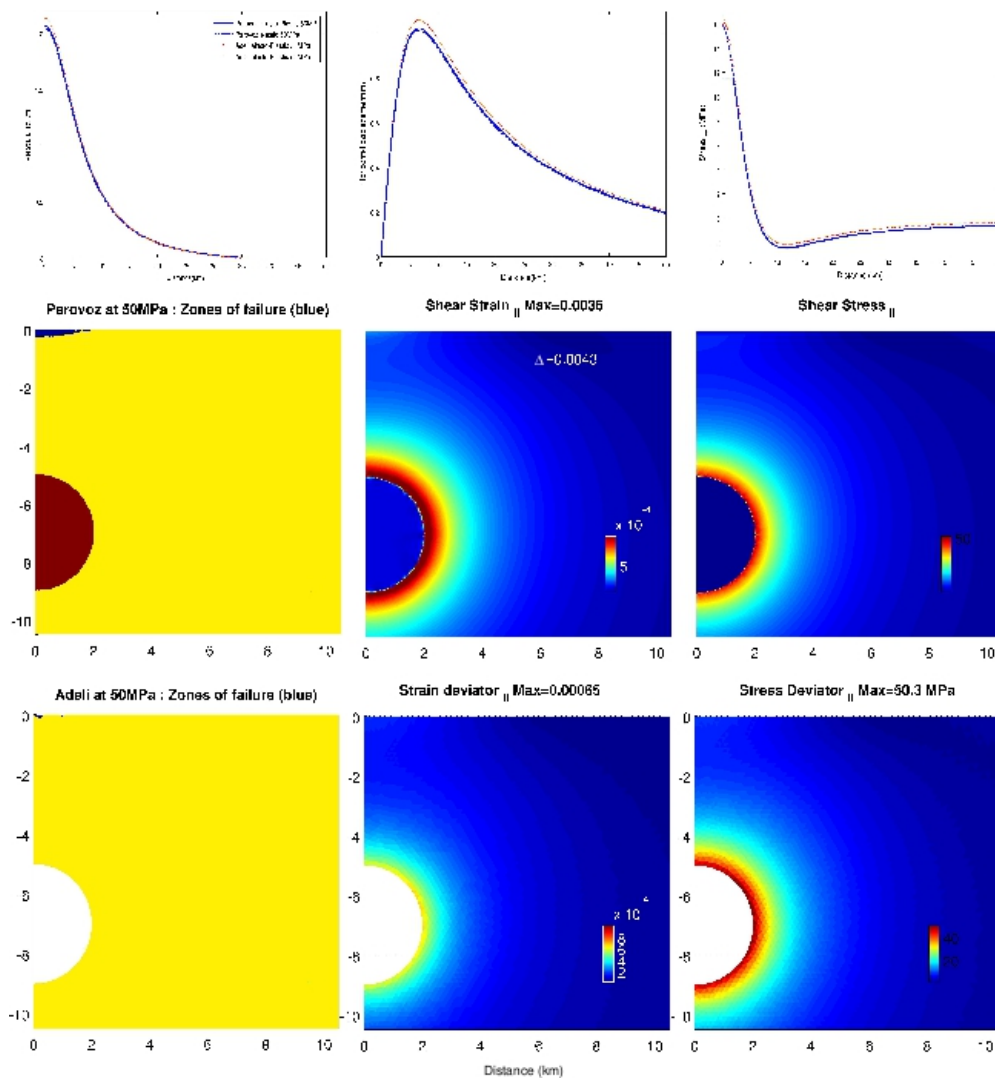


Fig. A1.

In general, modeled surface displacements are greater in Adeli than in Parovoz by about 5% (maximum uplift of 2.13 m versus 2.05 m, Table 1). We attribute this difference to the combined effect of the emptiness of the chamber in Adeli, and local numerical discontinuities at the stair-shape wall geometry of the chamber in Parovoz, which increase the shear strain there.

## **A2) Benchmarks for a mostly plastic domain, $\Delta P=120\text{MPa}$**

Now we compare results between Parovoz and Adeli for an internal overpressure of  $\Delta P=120\text{MPa}$ , so that the domain in between the chamber and the ground surface is in majority at a state of plastic yield. In this case, the chamber's wall mesh elements are progressively submitted to a stress level much above their yield stress, therefore numerical artifacts are expected to be favored here.

We observe in Fig. A2.(top) that modeled surface displacements and stress with Parovoz are generally smaller than those obtained with Adeli, again by about 5% (e.g. Table 1). The failure domain in Parovoz has a greater extent than in Adeli at  $\Delta P=120\text{ MPa}$ . However, very good consistency is seen in between the Parovoz model at  $\Delta P=120\text{ MPa}$  and the Adeli model at  $\Delta P=150\text{ Mpa}$  (Figure A2, bottom). From additional models with frictionless material (not shown here), we believe that these differences are partly related to the different algorithmic procedures for plastic yielding employed in Parovoz and Adeli (explicit Mohr-Coulomb versus implicit Drucker-Praeger in Adeli).

## **A3) Benchmarks without gravity $\Delta P= 15$ and $18\text{ MPa}$**

Models without gravity (equivalent to a state of lithostatic pore fluid pressure) are also compared with Parovoz and Adeli. For  $\Delta P =15\text{ MPa}$ , surface displacements and horizontal stress are in extremely good agreement (Fig. A3, top). However, the failure pattern occurs over a circular domain around the chamber significantly thinner with Adeli than with Parovoz (middle figures in Fig. A3). We also plotted failure patterns which look very similar, and correspond to  $\Delta P=18.1\text{ MPa}$  in Parovoz and  $\Delta P =18.9\text{ MPa}$  in Adeli (bottom lines in Fig. A3). Note, as in Fig. A2, the peculiar ear shape of the plastified domain, which is similar to that obtained in other studies (e.g. Massinas & Sakellariou, 2009, Fig. 2d, or Chery et al., 1991).

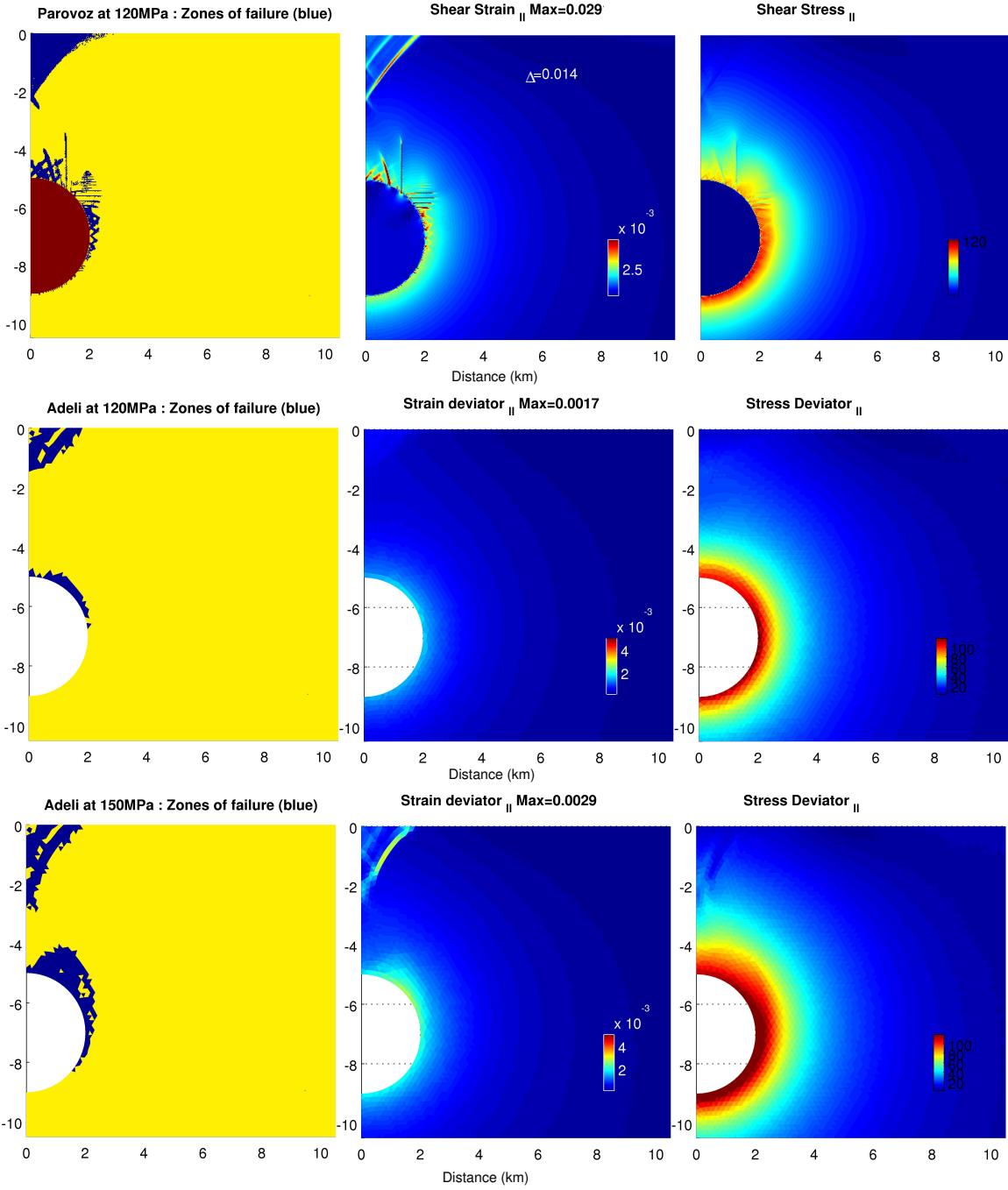
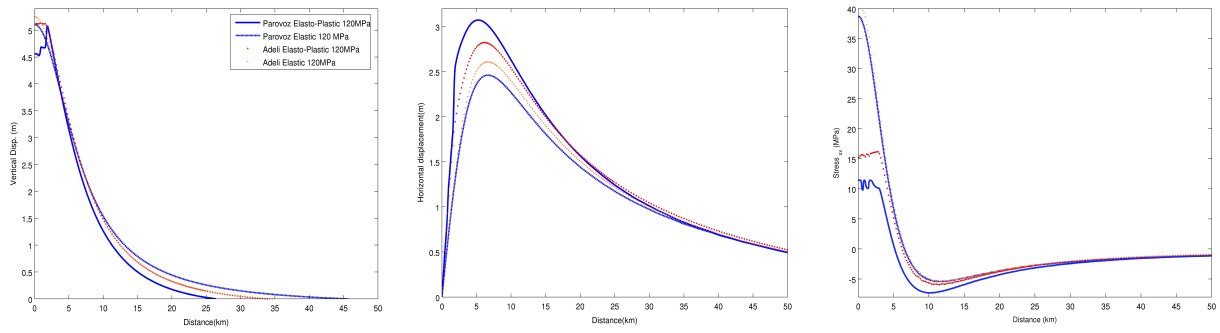


Fig. A2

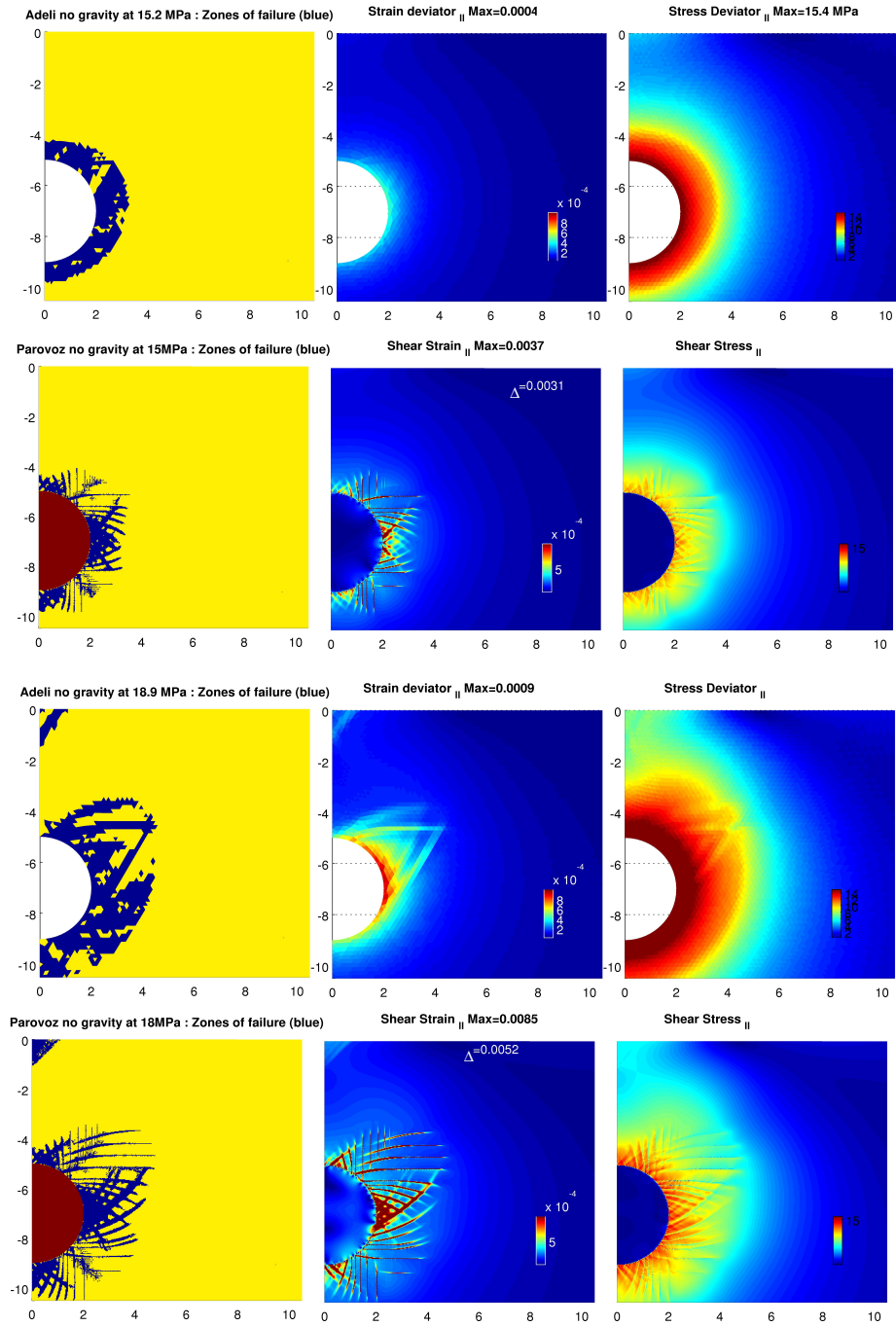
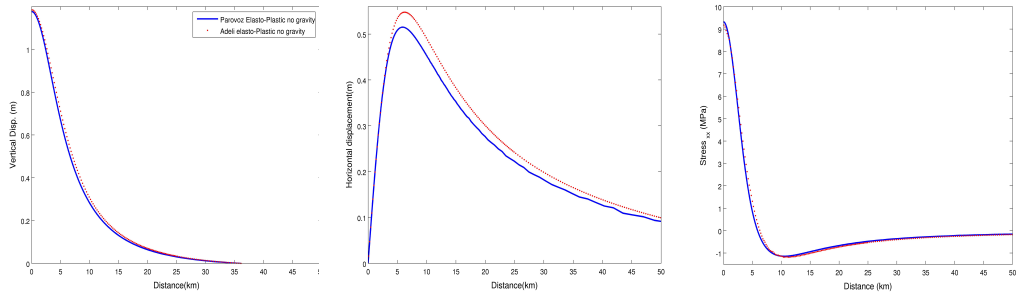


Fig. A3.

In conclusion, this benchmark shows a relatively good consistency of the model results obtained with Parovoz and with Adeli, considering that differences obviously rise from different mesh resolutions, mesh geometries (meshed versus unmeshed chamber), and numerical handling of constitutive laws. In order to obtain a better mechanical solution relieved from numerical artefacts, additional comparisons with other numerical tools throughout the community would be necessary. A collective project such as that developed to compare the geometry of faults in thrust nappes (Buiter et al., 2008) would be recommended. This latter benchmark showed that whereas results are qualitatively similar, it remains difficult to match shear band geometries exactly, since the highly non-linear process of failure depends on specific formulations used in each numerical method (e.g. Kaus, 2010; Yarushina et al., 2010).